Improving the quality factor of coaxial quarterwave resonators

Paul Heidler

November 2019
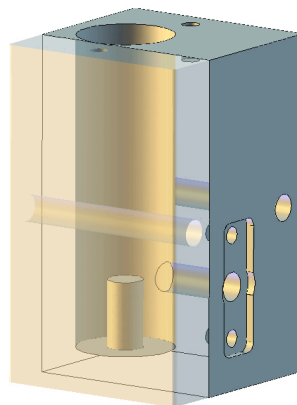
Supervised by Prof. Dr. Gerhard Kirchmair
Institute of Experimental Physics
University of Innsbruck
Austria

Abstract

In this thesis, three dimensional microwave cavities, more specifically coaxial $\lambda/4$ resonators, are investigated. The resonators are fabricated from three different metals: copper, aluminum and niobium. In order to achieve high quality factors, various surface treatments including chemical etching and annealing are applied. The particular resonator architecture, combined with the superconductor niobium, yields internal quality factors exceeding a billion (10^9) in a measurement environment of about $20\,\mathrm{mK}$.

For the normal conducting copper cavities $Q_{\mathrm{int}} \geq 10^4$, after the etching and annealing surface treatment, is reached. The high purity aluminum resonators achieve internal quality factors up to $\sim 10^7$, where a slight dependence on the cavity input power is detected. The niobium cavity shows an internal quality factor of $Q_{\mathrm{int}} \approx 0.5 \cdot 10^9$ at the single photon level and $Q_{\mathrm{int}} \approx 1.2 \cdot 10^9$ in the high drive power regime. This represents the highest-Q coaxial quarterwave resonator yet reported and corresponds to photon lifetimes in the range of $10 - 24\,\mathrm{ms}$. The increase of Q_{int}, while increasing either the temperature or the drive power, indicate that saturable two-level-systems, residing in the cavity wall's niobium oxide layer, are the dominating loss mechanism.

Besides extracting the resonator's quality factors with a scattering parameter reflection measurement in the frequency domain, an equivalent measurement method in the time domain is examined. Therefore the cavity reflected power is recorded, while applying a resonant drive pulse. The loaded quality factor Q_{l} is obtained from the cavity power decay. From the distinct shape of the transient behaviour, conclusions on the coupling regime can be drawn. Furthermore, an analytic expression for the reflected power response is derived, including the case of a detuned cavity drive. A fit of the cavity reflected power ring-up trace yields the resonator's characteristic parameters.

Acknowledgements

I had the fortune to spend time with amazing people in the course of this research. I want to thank my supervisor Gerhard Kirchmair for giving me the opportunity to conduct my master thesis in his research group. His spectacular enthusiasm about new experiments keep all group members motivated. Christian Schneider provided help at any time, even with error calculation code tutorials via skype from Boulder, Colorado. David Zöpfl always showed interest in my recent resonator developments, in my side projects, and always showed me pictures of his recent weekend trip. I owe a great debt to Max Zanner for his life lessons during coffee breaks. His open minded attitude is highly appreciated in the institute. I want to thank Oscar Gargiulo for showing me how to treat low noise amplifiers without grilling them. His Italian, to be exact Neapolitan treats made rough days turn bright. Stefan Oleschko introduced me with his accurate way of working into the art of aluminum etching. I am indebted to Aleksei Sharafiev, who patiently explained to me the phenomena of superradiance at the weirdest office hours. Mathieu Juan has a catching, science-thirsty vibe. Discussions with him, especially about data fitting were always productive.

I want to thank Gabriel Julian Partl for doing the rather nasty job of the niobium cavity buffered chemical polishing and Andrea Auer for the copper cavity annealing. Andreas Strasser, the great man behind the machines, always provided the best solutions for new cavity materials and geometry modifications.

Thank you Raffael Rabl for the golden times, either at the Seegrube, in front of the -50% supermarket shelf, or sitting back to back at our desks at IQOQI south. You are the man. Special shoutouts to my band Gilewicz, to the alte Hungerburg talstation, to the konnex/yakamoz society and to my brothers in Vienna for keeping me busy beside my master studies.

Finally, I want to thank my parents and my grandmother for their love and support through all those years studying. Most importantly, I want to thank Tatjana Heisinger, the sunshine of my life, who has been part of this journey since the beginning, for always being at my side.

Contents

1   Introduction

Superconducting circuits are one of the most promising platforms for quantum information processing [1]. Combining Josephson Junction based artificial atoms with microwave cavities depicts a promising direction for quantum computation and communication [2]. In the field of circuit quantum electrodynamics (cQED), microwave resonators are an essential building block for qubit readout [3] and qubit coupling [4].

Embedded in such systems, the qubit coherence time improved up to one hundred microseconds [5], which enables high-fidelity gate operations and puts the superconducting qubit approach near the error threshold required for fault-tolerant quantum computing [6].

Microwave resonators are especially interesting for quantum state storage. A transmon qubit embedded in a three dimensional microwave cavity, which is used as a quantum memory, can lead to lifetimes and coherence times in the millisecond range [7]. Therefore the qubit state is transferred into a non-classical photonic state, which circumvents the lifetime limitations of the superconducting qubit.

By further enhancing the quality factor of microwave resonators, particularly in the single photon drive strength regime, even higher photonic lifetimes can be generated. At these low cavity input power levels, dissipation mechanisms concerning a lossy dielectric layer on the cavity surface have to be faced [8]. Additionally, a finite surface resistance of the superconducting cavity, e.g. due to material defects, can be a limiting factor. Using the strategy of either lowering the resonator's sensitivity to the loss mechanism or improving the condition of the cavity surface, a comprehensive loss reduction is feasible. Extending the photonic lifetime of coaxial $\lambda/4$ resonators represents the aim of this thesis.

2 Microwave resonators

This chapter gives an introduction to the main concepts that characterise microwave resonators. The focus will be on resonators in reflection configuration, as it is the scenario used in the experiment. A profound discussion on radiofrequency and microwave engineering can be found in [9]. A detailed analysis about quality factors and loss mechanisms in microwave resonators is given in [10]. A study on scattering matrix elements for microwave resonator networks in either notch or refelction configuration is covered in [11–13].

2.1 Definition of quality factors and participation ratios

An important parameter characterising the losses of a resonator is the quality factor. It is defined as

$$Q = \omega_0 \, \frac{\text{Total energy stored}}{\text{Total power dissipated}} = \frac{\omega_0}{\kappa} \tag{2.1}$$

with the resonance frequency ω_0 and the energy decay rate κ [10]. Since many loss mechanisms contribute to the total, or loaded quality factor Q_l, a division into external or coupling losses and internal losses proved useful. The coupling quality factor Q_c describes the resonator's energy dissipation to an external circuit, which is used for measuring the resonator. The internal quality factor involves the resonator's intrinsic losses, for instance due to a resistive conductor or a lossy dielectric layer on the metal surface. The loaded quality factor is defined as the reciprocal sum of internal and coupling quality factor

$$\frac{1}{Q_l} = \frac{1}{Q_c} + \frac{1}{Q_{\text{int}}} \tag{2.2}$$

Q_l is limited by the dominating loss channel. Therefore three coupling regime scenarios (see table 2.1), depending on the ratio of Q_{int} and Q_c, can be distinguished. A useful tool to investigate a resonator's sensitivity to various intrinsic

Table 2.1: Overview of the different coupling regimes.

$Q_c > Q_{\text{int}}$	under-coupled
$Q_c \approx Q_{\text{int}}$	critically coupled
$Q_c < Q_{\text{int}}$	over-coupled

loss mechanisms is to inspect its participation ratios [10], which are defined as

$$p_n = \frac{\text{Amount of energy sensitive to loss mechanism}}{\text{Total energy stored}} \tag{2.3}$$

Each loss mechanism brings along a participation ratio that depends strongly on the resonator geometry. Calculating the participation ratios leads to an estimation for the limits of a certain resonator design. The corresponding quality factors are given by

$$Q_n = \frac{1}{p_n \tan \delta_n} \tag{2.4}$$

The material property $\tan \delta_n$ depicts the loss tangent, which is a parameter sensing how lossy a certain mechanism acts.

2.2   Scattering parameter
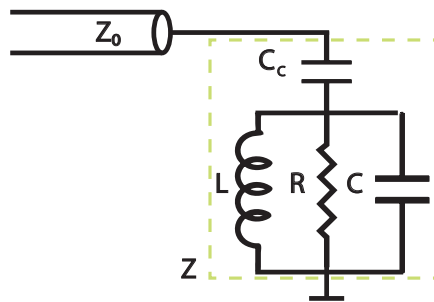
Figure 2.1: Schematic of the equivalent circuit of a resonator in the single port reflection configuration. The resonator itself is modelled as a parallel LRC-circuit, which is capacitively coupled (C_c) to an open ended transmission line with the characteristic impedance Z_0. The LRC-circuit and the coupling capacity C_c are summarised to an input impedance Z.

The measurement of a resonator in reflection configuration can be modelled with the equivalent circuit depicted in figure 2.1. An open-ended transmission line with the characteristic impedance Z_0 connects the resonator, which is represented by a parallel LRC-circuit, to the outside world through a coupling capacitor C_c. The resonator and its coupling capacitor can be combined to an input impedance Z. Following [12], the input impedance seen by the transmission line near resonance $\Delta\omega \ll \omega_0$ becomes

$$Z(\omega) = Z_0 \left(\frac{Q_c}{Q_{\text{int}}} + j\frac{\Delta\omega}{\omega_0}2Q_c \right) \tag{2.5}$$

The change of impedance seen by an incoming signal V_{in} causes a reflection following

$$V_{out} = S_{11}V_{in} \tag{2.6}$$

where V_{out} describes the reflected signal and S_{11} the reflection scattering parameter

$$S_{11} = \frac{Z - Z_0}{Z + Z_0} \tag{2.7}$$

The resulting formula characterising a resonator in the single port reflection scenario is

$$S_{11}(\omega) = 1 - \frac{2Q_l/Q_c}{1 + 2jQ_l\frac{\Delta\omega}{\omega_0}} \tag{2.8}$$

The scattering parameter S_{11} corresponds to a circle in the complex plane with distinct characteristics in each coupling regime. The absolute square $|S_{11}(\omega)|^2$ forms an inverse Lorentzian centered at ω_0 with the full-width-half-maximum $\kappa = \omega_0/Q_l$. Further explication on the extraction of the resonator properties from a S_{11} measurement are given in section 4.2.

3   The coaxial $\lambda/4$ resonator

In this chapter the properties of the coaxial $\lambda/4$ resonator are investigated. The advantages of the cavity geometry, the coupling to the cavity and its loss mechanisms are discussed. The concept of the high-Q coaxial quarterwave resonator was developed by Reagor et al. [7]. The discussion is based on [10].

3.1   Features of the resonator design

The coaxial $\lambda/4$ resonator is designed to accomplish high quality factors. The key element of the cavity geometry concept is to combine a circular waveguide with a coaxial transmission line, which is short circuited at the bottom and terminated in an open circuit at the top end. An illustration of the cavity design is given in figure 3.1. The length l' of the remaining stub defines the resonators resonance condition. The fundamental resonance frequency is approximately given by $l' \approx \lambda/4$, the next transmission line mode is expected to be at $l' \approx 3\lambda/4$. The capacitive loading at the top of the stub changes the mode's resonance frequency, estimated by the stub's length condition, to lower values. The big gap between the fundamental and the higher modes ensures the exclusive excitation of the fundamental mode in a measurement. The electric field is at its maximum at the top of the stub, and decreases down to the bottom end. The outer conductor of the coaxial transmission line merges above the stub into the circular waveguide section, which is closed on top with a light tight seal. The waveguide transmits modes above its cutoff frequency f_c, but suppresses the transmission of modes below f_c exponentially. This circumstance is used, as the length of the stub and further the resonance frequency is chosen to be below cutoff $f_0 \ll f_c$. The fields of the fundamental resonator mode are exponentially attenuated in the waveguide section. High internal quality factors are achieved, since the contact resistance is substantially lower at the top of the circular waveguide.

The fields of the TEM modes of a coaxial transmission line are given in cylindrical coordinates by

$$\vec{E} = \frac{V_0 \cdot \hat{\rho}}{\rho \cdot \ln b/a}\, e^{-\beta z} \tag{3.1}$$

$$\vec{H} = \frac{V_0 \cdot \hat{\phi}}{\rho \cdot \eta \ln b/a}\, e^{-\beta z} \tag{3.2}$$

with the line's inner and outer conductor radii a and b, the propagation constant β, the voltage amplitude V_0 and the wave impedance $\eta = \sqrt{\mu/\epsilon}$ [9]. The variables
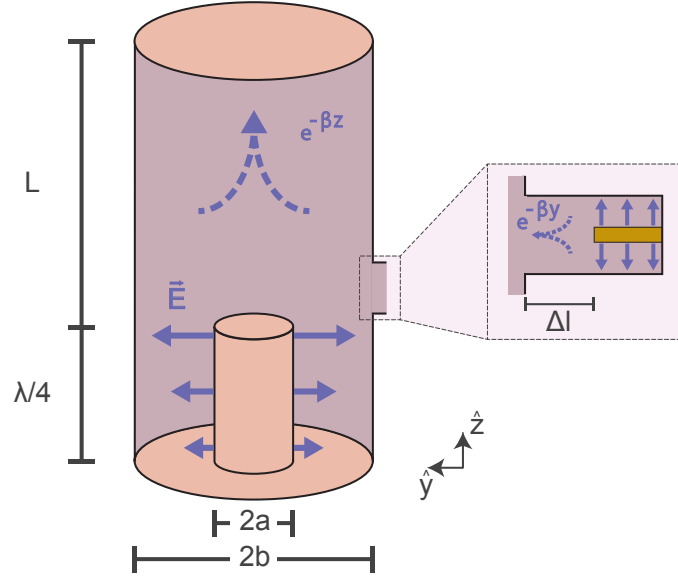
Figure 3.1: Design of the high-Q coaxial $\lambda/4$ microwave resonator. The cavity can be divided into three sections: the circular waveguide section of length L and radius b, a coaxial transmission line of length $\lambda/4$ and inner and outer conductor radii a and b, which is short circuited at the bottom and open circuited at the top end of the stub, and the sideways coupling section. The coupling section involves a coupling pin, with a distance Δl between the end of the pin and the actual resonator. The space in between represents another a circular waveguide. Fields in circular waveguides below the cutoff frequency are attenuated as indicated in the drawing.

μ and ϵ depict the permeability and permittivity of dielectric material in between the conductors. The radii of the inner and outer conductor are primarily chosen to be $a = 2\,\text{mm}$ and $b = 5.25\,\text{mm}$, due to machining restrictions. After changing to the sinker electrical discharge machnining technique, the radii are altered slightly to accomplish ratio $a : b$ of $3 : 1$, which minimizes the surface resistance losses [14]. The height of the stub is chosen to be 8mm, which corresponds to a calculated frequency of 9.369 GHz. The resonator mode's electric field reaching into the waveguide, as seen in the simulated field plot in figure 3.2, causes a shunt capacitance and an effectively extended stub length, which results in an actual lower resonance frequency. Finite element simulations, done with the software

HFFS [15], predict a resonance frequency of 7.644 GHz for the first set of the coaxial radii a and b and considering perfectly conducting cavity walls.
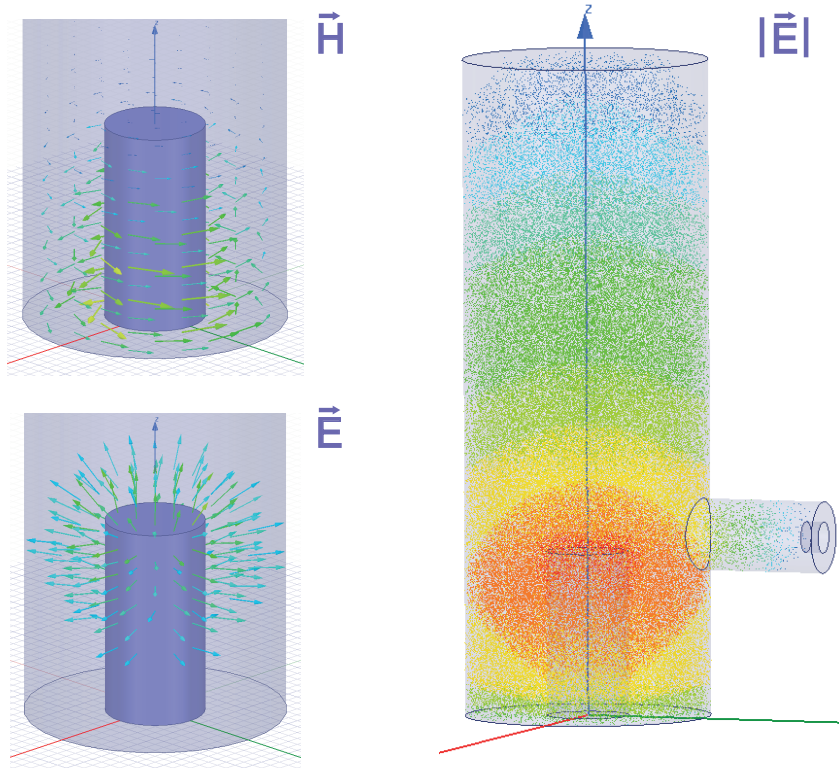
Figure 3.2: Fundamental mode field plot of the coaxial quarterwave resonator obtained from HFFS simulations. Shown is a vector plot of the magnetic field $\vec{H}$ and the electric field $\vec{E}$ in the area surrounding the stub. Furthermore the magnitude of the electric field $|\vec{E}|$ of the whole resonator is shown, where the decrease of the electric field energy along the waveguide section becomes visible.

The mode, that is most likely to set the resonators propagation into the waveguide, is the circular TM_{01} mode. It is favourable for the resonator geometry, as the electric and magnetic field distribution of the TEM cavity mode and the TM_{01} waveguide mode share great similarities (see figure 3.3). Both modes show magnetic field lines circling around the center and radially spread electric field lines. From all the TM modes the resonator couples to, the TM_{01} mode is the one with the lowest cutoff frequency. The propagation constant of the TM_{01} mode is given by

$$\beta = \sqrt{k^2 - k_c^2} = \sqrt{k^2 - \left(\frac{p_{01}}{b}\right)^2} \tag{3.3}$$

with the wavenumber $k = 2\pi/\lambda$ and the cutoff wavenumber k_c, the waveguide radius b and the first root $p_{01} = 2.405$ of the Bessel function J_0. The cutoff
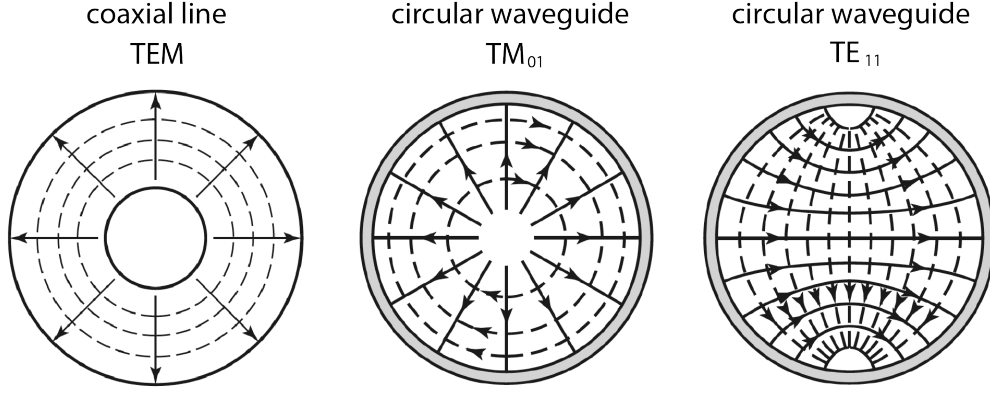
Figure 3.3: Electric (solid) and magnetic (dashed) field lines of the TEM mode in a coaxial line compared to the TM_{01} mode and the TE_{11} mode in a circular waveguide. From: [9, Chapter 3].

frequency of the circular waveguide is

$$f_c = \frac{c}{2\pi} k_c = 21.858 \, \text{GHz} \tag{3.4}$$

Since the cavity's resonance frequency is below cutoff, the propagation constant of the evanescent waveguide mode becomes a damping constant

$$\beta = \frac{j}{2.33} \, \text{mm}^{-1} \tag{3.5}$$

The electric field energy of the resonator mode decreases as

$$U_E \propto e^{-2\beta z} \tag{3.6}$$

along the z axis. By picking a circular waveguide length $L = 10/|\beta| \approx 23 \, \text{mm}$, the energy of the cavity mode is attenuated by roughly $e^{-20} \approx 2 \cdot 10^{-9}$. HFFS simulations shown in figure 3.4, assuming the cavity walls as perfect conductors and placing a port at the resonator's top that allows the leakage of the remaining resonator mode, confirm the exponential increase of the internal quality factor due to an extended waveguide section. Furthermore the simulations predict, that the resonator design with $L \approx 23 \, \text{mm}$, disregarding other loss mechanisms, should lead to internal quality factors of roughly 10^9.

Concerns that the TE_{11} mode (see figure 3.3), which includes a lower cutoff frequency than the TM_{01} mode, could play a role in the waveguide coupling, e.g. in case of an imperfect symmetry, are addressed by increasing the waveguide length to $L = 10/|\beta| \approx 33 \, \text{mm}$. This implies a field energy attenuating factor of about e^{-20}, calculated with the TE_{11} mode.

13
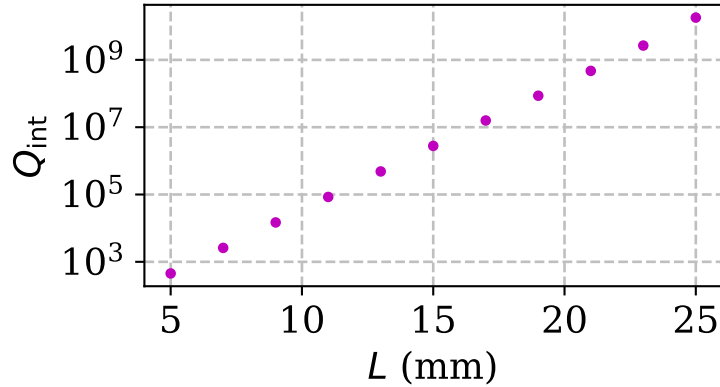
Figure 3.4: Simulated Q_{int} results demonstrate the exponential quality factor increase of a coaxial quarterwave resonator, while extending the length L of the waveguide section. As the cavity material is set to a perfect electric conductor, other internal loss mechanisms are neglected.

3.2   Coupling to the cavity

The cavity coupling is realized via a lateral channel, as shown in figure 3.1. The microwave signal enters the cavity via a copper coupling pin, which acts as a prolonged inner conductor of a coaxial cable. The copper piece is plugged into a SMA-connector and attached to the outer cavity wall. In this way the pin is aligned centrally in the cylindrical coupling tunnel. The pin and the cylindrical hole form a coaxial transmission line, which is continued by a circular waveguide at the end of the pin. The diameter of the pin and the coupling tunnel are chosen to achieve a characteristic impedance of $50\,\Omega$, which minimzes unintended signal reflections. The characteristic impedance of a coaxial transmission line follows [9]

$$Z_0 = \frac{1}{2\pi}\sqrt{\frac{\mu}{\epsilon}}\log\frac{D}{d} \tag{3.7}$$

As a consequence, the diameters are chosen to be $D = 3.5\,\text{mm}$ and $d = 1.5\,\text{mm}$. The TEM mode of the incoming signal is transferred at the end of the pin into a propagating wave in the circular waveguide. The frequency of the incoming signal is below the high waveguide's cutoff frequency of about 35GHz due to the small coupling tunnel diameter. Hence the signal towards the coupling pin is attenuated exponentially. This happens in a similar manner as the resonator waveguide coupling discussed previously. The distance between the end of the coupling pin and the actual resonator Δl determines the coupling quality factor. A proportionality can be stated with

$$Q_c \propto e^{2\beta\Delta l} \tag{3.8}$$

HFFS simulations confirm the exponential behaviour of Q_c depending on the distance Δl. The simulated results for the coupling quality factor with regards to a varying Δl, shown in figure 3.5, act as a reference to adjust Q_c in the experiment to the desired value.

Raising the coupling section in the upwards z-direction has the same effect on the coupling quality factor as shortening the pin. The center of the coupling tunnel is located $1\,\text{mm}$ above the top of the $\lambda/4$ stub.
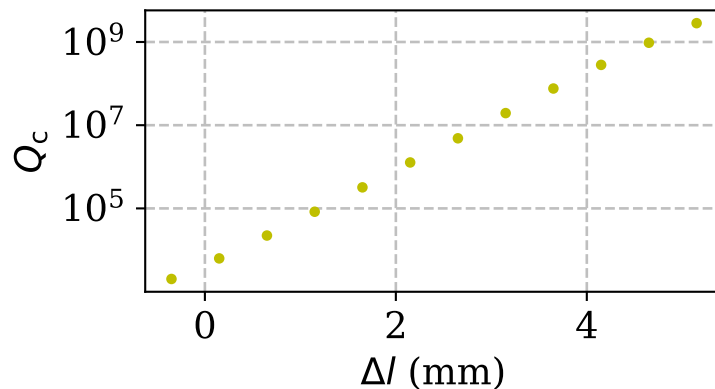
Figure 3.5: Simulated Q_c results for an increasing distance Δl between the end of the coupling pin and the actual resonator.

3.3   Internal loss mechanisms

In this section the internal losses of the high-Q stub resonator are further investigated. Therefore the participation ratios are calculated [10].

3.3.1   Dielectric loss

A part of the electric energy of the resonator mode is stored in a lossy dielectric layer on the surface of the cavity walls. The energy dissipation happens in the oxide layer on top of the conducting metals. The dielectric participation ratio is given by

$$p_{diel} = \frac{\epsilon \int_{\text{diel}} |E|^2 \, dV}{\epsilon \int_{\text{tot}} |E|^2 \, dV} \tag{3.9}$$

The ratio represents the electric energy stored in the dielectric divided by the total electric energy stored in the resonator. With some considerations, one can simplify equation 3.9. Only the perpendicular E-field components at the surface layer have to be considered, since on a superconducting metal surface the tangential electric field components disappear. Due to the continuity of the

electric field, the electric field in the surface layer has to match the electric field in the resonator volume $\vec{E}_{\text{vol}}$ under the condition

$$\vec{E}_{\text{surf}}\epsilon_{\text{surf}} = \vec{E}_{\text{vol}}\epsilon_{\text{vol}} \tag{3.10}$$

With the the oxide layer thickness t_{ox} and the relativ permettivity ϵ_r one can approximate the dielectric participation ratio to

$$p_{diel} \approx \frac{t_{ox} \int_{\text{surf}} |E_{vol}|^2 \, dA}{\epsilon_r \int_{\text{tot}} |E_{vol}|^2 \, dV} \tag{3.11}$$

Evaluating the integrals with the fields from equation 3.1 leads to

$$p_{diel} \approx \frac{t_{ox}}{\epsilon_r} \frac{2(a+b)}{(b^2 - a^2)} \tag{3.12}$$

The total dielectric quality factor is given by

$$Q_{diel} = \frac{1}{\tan \delta \, p_{diel}} \tag{3.13}$$

where $\tan \delta$ corresponds to the dielectric loss tangent. With the radii $a = 2\text{mm}$ and $b = 5.25\text{mm}$ the dielectric participation ratio results in $p_{diel} \approx 1.85 \cdot 10^{-7}$. The surface dielectric constant and layer thickness $\epsilon_r = 10$ and $t_{ox} = 3\,\text{nm}$ are taken from planar resonator measurements [16]. With an expected dielectric loss tangent $\tan \delta \leq 10^{-3}$, one can estimate the total dielectric quality factor $Q_{diel} \geq 10^9$.

3.3.2   Conductor loss

Conductor loss is the main loss mechanism for microwave cavities made out of normal metals. But also the quality factor of superconducting resonators can be dominated by losses due to a finite surface resistance. The total magnetic quality factor is given by [8]

$$Q_{mag} = \frac{\omega \mu_0 \delta}{R_s} \cdot \frac{1}{p_{mag}} \tag{3.14}$$

with the surface resistance R_s, the surface reactance $X_s = \omega \mu_0 \delta$ and the magnetic participation ratio

$$p_{mag} = \frac{\delta \int_{\text{surf}} |H|^2 \, dA}{\int_{\text{tot}} |H|^2 \, dV} \tag{3.15}$$

where δ depicts the resonator material's skin depth. Evaluating the integrals for the coaxial quarterwave resonator with the fields from equation 3.1 gives

$$p_{mag} = \frac{\delta}{ln(b/a)} \cdot (\frac{1}{a} + \frac{1}{b}) \tag{3.16}$$

Minimizing 3.16 results in an ideal coaxial cunductor radius ratio $b/a \approx 3.59$, which deviates a bit from the $3:1$ ratio stated in [14]. Inserting the radii $a = 2$mm and $b = 5.25$mm, the magnetic participation ratio yields in $p_{mag} \approx 715 \cdot \delta$. For a superconducting metal, δ is replaced by the penetration depth λ. Using the penetration depth $\lambda \approx 50$ nm of the superconducting aluminum [8], the magnetic participation ratio becomes $p_{mag} \approx 3.6 \cdot 10^{-5}$. For a copper coaxial resonator, with $X_s/R_s = 1$ and $\delta = 660$ nm [9], the room temperature total magnetic quality factor can be estimated by $Q_{mag} \approx 2000$. Considering a typical ratio $X_s/R_s \approx 2 \cdot 10^5$, achieved with superconducting niobium cavities [16], the total magnetic quality factor amounts to $Q_{mag} \approx 5 \cdot 10^9$.

4   Frequency domain measurements

4.1   Experimental setup

A sketch of the experimental setup is shown in figure 4.1. A vector network analyzer operates as both, signal generating and analyzing device. The measured scattering parameter is the ratio of the VNA's input to output voltage. The generated microwave probe signal leaves the VNA at port 1 and enters a dilution refrigerator. Inside the cryostat, there are different cooling stages. The cavity is mounted on a copper bracket at the base plate, where temperatures down to 20 mK are achievable. Coaxial cables act as transmission lines to transfer the signal from the VNA to the resonator and back. To thermalize the input signal, cryogenic attenuators of 20 dB at the 4 K stage and 30 dB at the base plate are assembled. The combination of an Eccosorb and a DC to 12 GHz lowpass filter help to reduce noise at higher frequencies. After passing a circulator, the input signal approaches the cavity. The circulator is a three way device, that routes the signal in one direction from one port to the other, with a bit of leakage in the backward direction. This way the cavity reflected signal can be measured through an output line. Although the cavity reflected signal leaves the cryostat through another transmission line, it is practically a reflection measurement. The resonator is housed in an additional mu-metal shield, which provides a further protected environment from magnetic fields. The cavity output signal passes the circulator and is led through two isolators. An isolator is a similar device as a circulator, where one port is terminated with a 50 Ω load. The cavity reflected signal is amplified by a low noise high electron mobility transistor (HEMT) amplifier at the 4 K stage. This amplifier ensures a gain of 40 dB in the desired frequency range. The Isolators, which are mounted before the HEMT stage, are typically needed to prevent HEMT noise going back to the experiment. The output signal is amplified once again at room temperature and then guided into the second port of the VNA.

A picture of the experimental setup inside the cryostat is shown in appendix A.

Microwave switch

Since a large number of available output lines is a rare event in the daily lab business, the implementation of a microwave switch can maintain the good atmosphere between research colleagues. Furthermore, cryostat cool-down and warm-up cycles can be reduced. A switch mounted in between the cavity and the

circulator allows the measurement of multiple cavities within a single cool-down using one pair of input and output lines. The *Radiall* switch SP6T R573423600 distributes one common microwave input channel into six outputs. It has to be modified to ensure oparability in a cryogenic environment, following [17]. After the removal of the switch's shield the printed circuit board is disassembled. The remaining, fragile connectors to each channel's coil are strengthened with the epoxy glue *Stycast*. The modified switch is mounted on the base plate of the cryostat. The current supply is established linking each coils connector to the fridge's DC lines, which are further connected to a current source. By applying a current pulse of about $160\,\mu$A for $10\,$ms to one channel's coil, the induced magnetic field shifts an actuator and establishes the microwave connection. A current pulse with an inverted direction breaks the microwave connection. Every switch event generates heat, since the coils are made of resistive copper. This displays a disadvantages of the use of a microwave switch, because most of the measurements in the cryostat have to be paused after switching until the initial temperature is reached. Depending on the strength of the current pulse, the cryostat heating ranges from tens to a few hundreds of mK, where the corresponding re-cooling can take up to few hours. The bigger inconvenience is the problem of static discharges inside the input stage of the HEMTs, caused by a DC pulse forwarded onto the microwave signal. Inner and outer DC blocks mounted before and after the switch should prevent damage on the HEMTs and other measurement devices while switching. Nevertheless, plugging out the VNA and the HEMT power supply before switching proofed to be beneficial, since a repair tends to be expensive and time consuming.
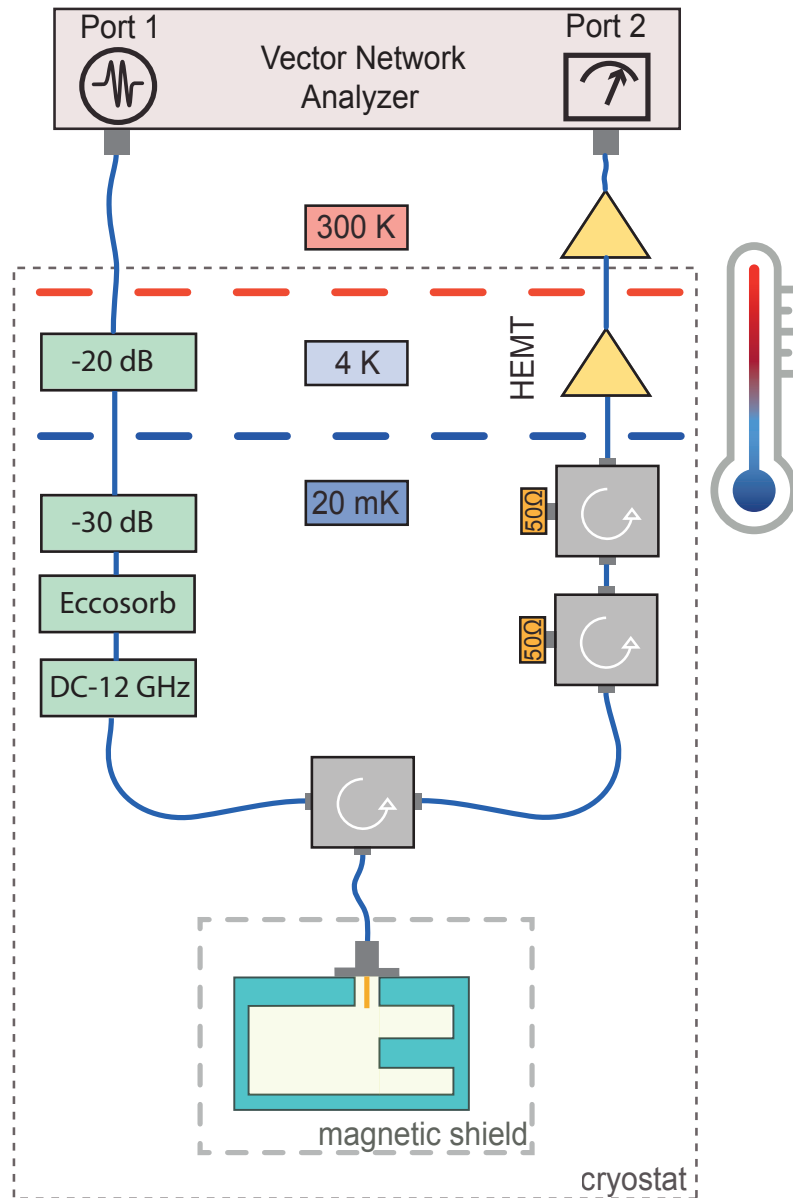
Figure 4.1: Schematic of the experimental setup. The cavity's performance is evaluated by a scattering parameter measurement done with a vector network analyzer. The VNA provides a microwave signal, which is forwarded through port 1 into the cryostat via a coaxial cable. A 20 dB attenuation at the 4 K plate and a 30 dB attenuation at the 20 mK base plate follow. After an eccosorb- and a DC to 12 GHz lowpass filter, the input signal arrives down at the resonator through a circulator. The cavity itself is mounted inside a magnetic shield. The reflected signal passes the circulator, two isolators and gets amplified twice (yellow triangles). First, by a high-electron-mobility transistor (HEMT) at the 4 K cooling stage and then by a room temperature amplifier after leaving the cryostat. The isolated and amplified cavity output signal is led into port 2 of the VNA.

4.2 Circle fit model for a resonator in reflection configuration

The circle fit routine was implemented by the group members David Zöpfl and Christian Schneider [18]. It was developed to extract the resonator parameters from a scattering parameter measurement. The scattering parameter for a resonator in the single port reflection scenario follows

$$S_{11}(\omega) = \frac{2Q_{\mathrm{l}}/Q_{\mathrm{c}}}{1 + 2jQ_{\mathrm{l}}\frac{\omega-\omega_0}{\omega_0}} - 1 \tag{4.1}$$

Note that equation 4.1 slightly differs from equation 2.8 presented earlier. The formula used for the circle fit describes an inverted circle in the complex plane compared to the model specified in [12], which is an equivalent approach. The absolute square of S_{11}, forming an Lorentzian of width κ, is not affected by the sign changes

$$|S_{11}(\omega)|^2 = 1 - \frac{1 - \frac{(2Q_{\mathrm{l}}-Q_{\mathrm{c}})^2}{Q_{\mathrm{c}}^2}}{1 + 4Q_{\mathrm{l}}^2(\frac{\omega-\omega_0}{\omega_0})^2} \tag{4.2}$$

The loaded quality factor Q_{l} defines the width κ of the resonance, the dip depth depends on the ratio of Q_{c} and Q_{int}. The phase $\Theta(\omega) = arg(S_{11}(\omega))$ follows

$$\Theta(\omega) = \arctan\left(\frac{4Q_{\mathrm{l}}\frac{\omega-\omega_0}{\omega_0}}{Q_{\mathrm{c}} - 2Q_{\mathrm{l}} + 4Q_{\mathrm{c}}Q_{\mathrm{l}}^2(\frac{\omega-\omega_0}{\omega_0})^2}\right) \tag{4.3}$$

In the over-coupled regime ($Q_{\mathrm{l}} = Q_{\mathrm{c}}$ and $Q_{\mathrm{int}} \to \infty$) equation 4.3 simplifies to

$$\Theta(\omega) = -2\arctan\left(2Q_{\mathrm{l}}\frac{\omega - \omega_0}{\omega_0}\right) \tag{4.4}$$

which corresponds to a full 2π phase shift. In the same coupling limited regime, the absolute square follows $|S_{11}(\omega)|^2 = 1$, as the lack of intrinsic losses causes all of the resonator's energy to reflect back. Heading for the under-coupled regime ($Q_{\mathrm{int}} < Q_{\mathrm{c}}$), the dip depth of the resonance decreases and the phase shift disappears, but a discontinuity around ω_0 remains. In the complex plane, $S_{11}(\omega)$ forms a circle of diameter $2Q_{\mathrm{l}}/Q_{\mathrm{c}}$. The off resonant point is located at -1 on the real axis. On resonance, the scattering parameter approaches $S_{11} \to 2Q_{\mathrm{l}}/Q_{\mathrm{c}} - 1$. In the cirtically coupled regime, the circle crosses the origin of the complex plane.

The circle fit routine utilizes the formula

$$S_{11}^{fit}(\omega) = (ae^{j(\alpha-\pi)}e^{-j\omega\tau})S_{11}(\omega) \tag{4.5}$$

21

which adds the measurement environment to the model. The paramters a and α account for additional attenuation and phase shift. Furthermore the effect of the cable delay τ, which increases linearly with the measurement frequency, is included. The main steps of the fit routine are shown in figure 4.2, where the circle fit is applied on measured S_{11} data of a superconducting aluminum coaxial $\lambda/4$ resonator.

At first, the cable delay in the phase signal and the linear background in the magnitude is extracted. A Lorentzian fit of $|S_{11}|^2$ results in inital Q_l and ω_0 values for the circle fit. An initial circle fit yields the attenuation constant a and the additional phase shift α from the environment. As a result of the phase fit, the circle's off resonant point is obtained. After including all environmental effects, the final normalized circle fit contains the resonator parameters Q_l, Q_c and ω_0. The internal quality factor Q_{int} is calculated subsequently. The errors of the resonator parameters are back propagated values from the fit error. Therefore the Jacobian Matrix, which contains the partial derivative of the circle fit function to each fit parameter, is combined with the fit residuals.

4.2.1 Average photon number calibration

The estimation of the average photon number $\langle n_{ph} \rangle$ circulating in the cavity on resonance corresponding to the input drive power P_{in} is done following [19]. The reflected power is given by

$$P_{refl} = P_{in}|S_{11}|^2 \tag{4.6}$$

The power absorbed from the resonator is

$$P_{abs} = P_{in} - P_{refl} = \frac{4Q_c Q_{\text{int}}}{(Q_c + Q_{\text{int}})^2}P_{in} \tag{4.7}$$

Another definition of the absorbed power in the resonator is

$$P_{abs} = \langle n_{ph} \rangle \hbar \omega_0 \frac{\omega_0}{Q_{\text{int}}} \tag{4.8}$$

The combination of the equations above results in

$$\langle n_{ph} \rangle = \frac{4}{\hbar \omega_0^2} \frac{Q_l^2}{Q_c} P_{in} \tag{4.9}$$

The interpretation of $\langle n_{ph} \rangle$ refers more to an upper limit, as it is difficult to include all reflections in the measurement line. The total attenuation from the signal generator down to the resonator, mounted on the base plate in the cryostat,

was evaluated to 69dB.
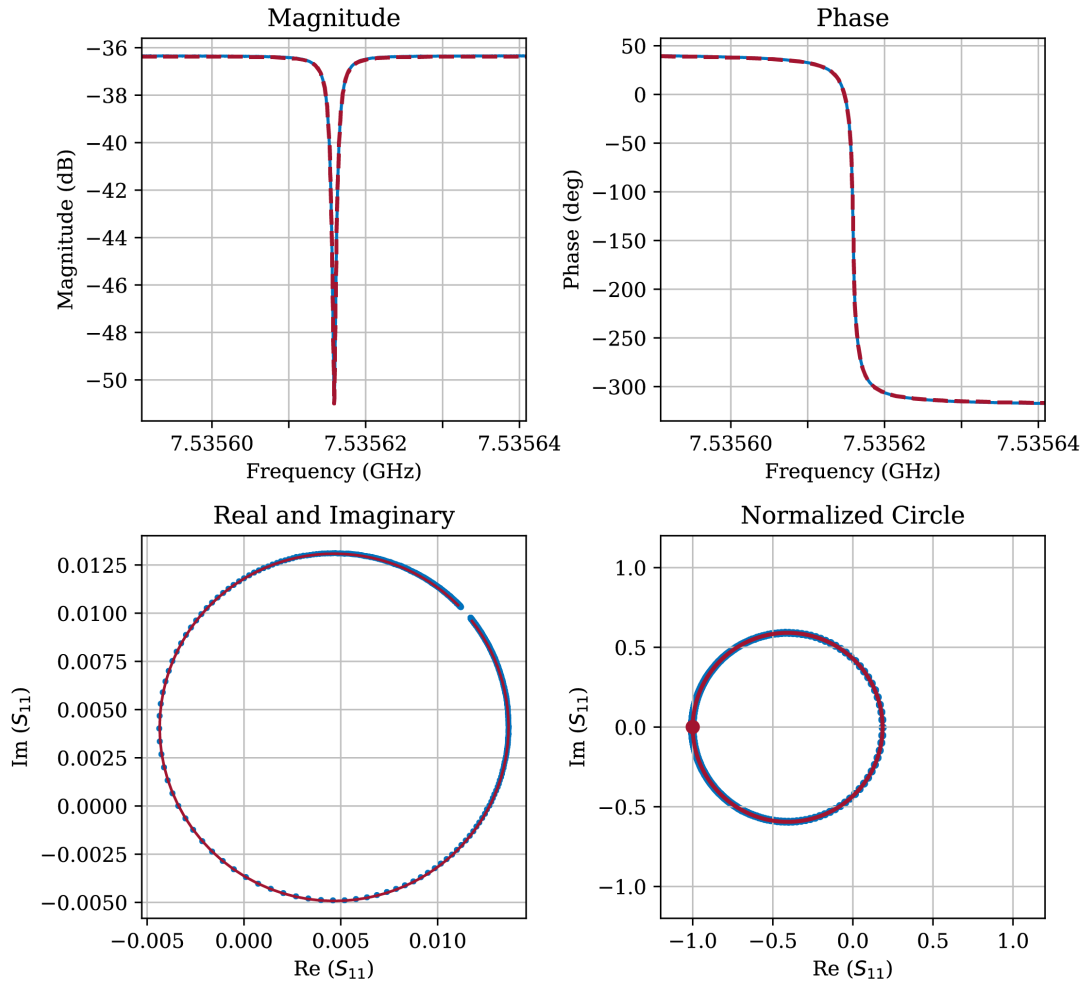
Figure 4.2: Circle fit of the measured S_{11} parameter of a superconducting aluminum coaxial quarterwave resonator. In the top panel the S_{11} magnitude (left) and phase (right) is shown. The measured data is marked blue, the fits are displayed in dashed red lines. In the lower left panel the initial circle fit on top of the measured S_{11} data in the complex plane is shown. The subtraction of all measurement environment effects results in a normalized circle (right), where the off resonant point is marked with a red dot.

4.3 Copper cavities

The coaxial quarterwave cavity design was first tested with three different purity grades of copper. The advantage of a high-Q normal conducting cavity would be the possibility to introduce magnetic fields, which is not possible with super-conductors due to the Meissner effect [20, chapter 13], while maintaining long photonic lifetimes. The challenging machining task of the stub on the ground of the resonator was realised using a special drill bit, which features a hollow tip. After lifting the drill from the bottom of the cavity, a stub of predefined dimensions remains. As described in section 3, the copper cavity's inner and outer diameter are $a = 2\,\mathrm{mm}$ and $b = 5.25\,\mathrm{mm}$, the stub length is $8\,\mathrm{mm}$. The copper purity grades range from 2N over 4N5 to 6N, where the Ns stand for the nines in the purity percentage. For example, 4N5 means $99,995\%$ pure. At room temperature, VNA circlefit measurements of the copper resonators show an internal quality factor ranging from approximately 1500 to 2500, depending on the purity grade. This is in agreement with the estimation done in section 3.15, assuming the main internal energy dissipation comes from conductor losses. To improve the surface resistance of the inner cavity walls, which were directly exposed to the machining process, the top layer ($\sim 100\mu\mathrm{m}$) gets removed by etching. Therefore metal impurities and defects introduced by the machining process should be reduced. With annealing the resonators, another strategy on improving surface characteristics is utilised. A picture of the different copper resonators after varying processing steps is shown in figure 4.3.
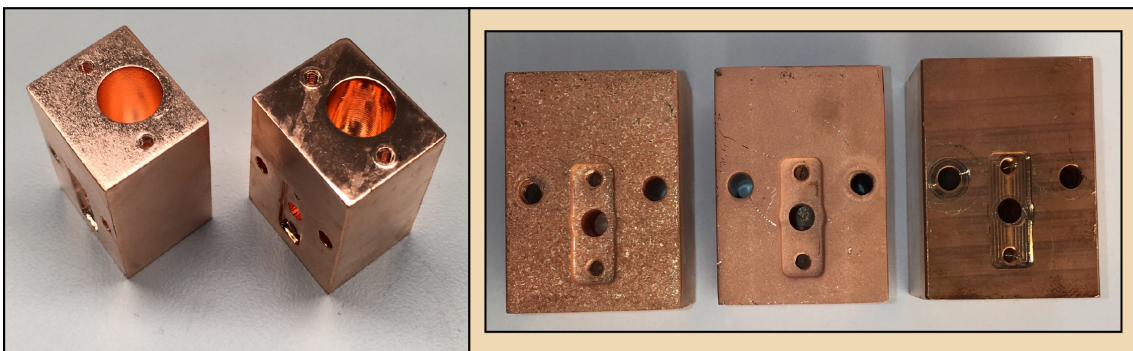
Figure 4.3: Picture of the copper coaxial $\lambda/4$ resonators of different purity grades after varying surface treatments. From left to right: annealed 2N and etched and annealed 6N; etched 2N, etched 4N5 and untreated 4N5.

4.3.1   Surface preparation

The copper cavity chemical etching is realised initially with ferric chloride ($FeCl_3$), which is an universal etchant for various metals like steel, aluminum, copper or nickel. The chemical reaction follows [21]

$$FeCl_3 + Cu \rightarrow FeCl_2 + CuCl \tag{4.10}$$

The ferric ions oxidize the copper, which results in the formation of cuprous chloride (CuCl) and ferrous chloride $FeCl_2$. The CuCl is further oxidized in the etchant producing $CuCl_2$

$$FeCl_3 + CuCl \rightarrow FeCl_2 + CuCl_2 \tag{4.11}$$

The generated $CuCl_2$ reacts itself with the copper surface following

$$CuCl_2 + Cu \rightarrow 2CuCl \tag{4.12}$$
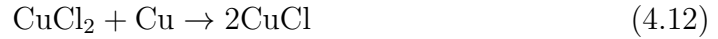
The etchant is generated by adding the iron salt $FeCl_3 + 6H_2O$ to distilled water. The etching temperature is chosen to be $25°$ C with a concentration of the etch solution of 2.5M [22], where the molarity M corresponds to the moles of the solute per volume of the solution in liters. Therefore 200 ml of distilled water are mixed with 135 g of $FeCl_3 + 6H_2O$ in a glass container. The container is placed on a hot plate inside a flow box. To keep a steady flow of the etchant, a magnetic stirrer is added. The copper cavity is placed in the acid bath, where the temperature is monitored with a thermometer. The 2N copper cavity showed a surface removal of about 65μm after 35min. Etching the 6N copper cavity in the similar setup lead to a surface removal of roughly $170-200\mu$m. The amount of surface removal is quantified by measuring the outside dimensions of the resonator with a caliper rule before and after the etch treatment.

The complex chemcial reaction forming Fe^{2+}, Cu^{2+} and Cu^+ behaves like two seperate etch meechanisms, with the main etchant $FeCl_3$ and the byproduct-tatchant $CuCl_2$. This affects the etchrate and the surface roughness [21]. The etching of the 6N copper cavity produced a poor surface quality, as depicted in figure 4.4. Eventhough a higher concentration of the $FeCl_3$ etch solution could lead to an improved surface finish, the surface preparation is altered to the more moderate copper etchant $CuCl_2$ [23]. The chemical reaction of copper and cupric chloride ($CuCl_2$) is already given in equation 4.12, as it is the last step of the $FeCl_3$ etch process. The $CuCl_2$ etching is conducted by adding 58.8 g of the green

crystalline dihydrate salt $CuCl_2 + 2H_2O$ to 150 ml of distilled water. This corresponds to a concentration of the etch solution of 2.3M. The temperature of the etchant is set to 50° C, which yielded a surface removal of $40 \mu m$ from the 2N copper cavity after 50min. The rather matt surface finish can be explained by a CuCl passivation film on the metal surface [22, 23]. The CuCl layer is a product of the reaction that slows down the etching process. Adding a small amount (usally 1% of the solution volume) of hydrochloric acid (HCl) to the etchant, should counteract the growth of a CuCl passivation film, as CuCl and HCl react and produce $CuCl_2$ [23]. The etching rate stayed roughly the same by addition of HCl to the etch solution. 70min of etching the 4N5 copper cavity resulted in $50 \mu m$ surface removal. Dipping the resonator in hydrochloric acid and further rinsing it with distilled water, acetone and isopropanol after the etching process reduced the CuCl layer on the surface.

Another strategy to improve the surface chracteristics of the copper resonators is heat treatment. Annealing involves thermally activated processes that can lead to a partial removal of material defects coming from plastic deformation [24]. The copper cavity annealing was conducted at the institute of physical chemistry of the University of Innsbruck. In two cycles, five copper cavities were annealed in the presence of a reduced oxygen pressure due to controlled H_2 gas flow. The first set of cavities was annealed for 22h at a temperature of 960° C, the second set for 13h at 900° C. The shiny surface of the annealed cavities, as seen in figure 4.3, indicates that the annealing process cleared the CuCl layer resulting from the etching process.

Figure 4.4: 6N copper cavity after 1h FeCl etch treatment. The impact of the inhomogeneous etching treatment can be seen in the rough and distorted surface.

4.3.2   Results

The resulting internal quality factors from VNA measurements at about $T = 20\,\text{mK}$ of the copper cavities after different surface treatments are summarised in table 4.1. Both, annealing and etching improved the quality factor of each resonator. The impact of the purity grade on Q_{int} becomes less important after either or both surface treatments. The quality factor improvement after solely annealing comes close to the benefit of both procedures. The cavities, which were annealed at $960°\,\text{C}$ for 22h show no significant improvement compared to the ones annealed at $900°\,\text{C}$ for 13h. No Q_{int} input power dependence is observed. This suggests that the copper cavities are still limited by conductive losses. HFFS simulations including a finite conductivity of the cavity walls predict internal quality factors of $Q_{\text{int}} \sim 11{-}20{\cdot}10^3$ for electrical conductivities $\sigma = 1{-}3{\cdot}10^9\,\text{S/m}$. For the typical room temperature value of the copper conductivity $\sigma = 58{\cdot}10^6\,\text{S/m}$ [9], simulations predict $Q_{\text{int}} = 2,9 \cdot 10^3$. This leads to estimated values for the residual resistance ratio

$$RRR = \frac{\sigma_{293K}}{\sigma_{20mK}} \tag{4.13}$$

ranging from $\sim 17{-}52$. Besides the rather poor obtained electric conductivities, the low quality factors refer as well to the higher magnetic participation ratio p_{mag} compared to cylindrical cavities [8]. Rectangular waveguide cavities, as the ones seen in [25], but made of 2N copper show higher internal quality factors of about $Q_{\text{int}} \sim 20 - 30 \cdot 10^3$ without any surface treatment after machining.

This prompts the conclusion that the geometrical design of the coaxial $\lambda/4$ resonator is predestined to reach high quality factors only using superconducting metals.

Table 4.1: Summary of the measured copper resonators internal quality factors at $T = 20\,\text{mK}$ after various surface treatments.

Purity	$Q_{\text{int}} \cdot 10^3$	$T_{\text{ann}}(\text{C})$	$t_{\text{ann}}(\text{h})$	Surface removal (μm)
2N (99%)	3.5	/	/	/
2N	10	/	/	~ 105
2N	13	900	13	unetched
2N	17	960	22	~ 105
4N5 (99.995%)	13	960	22	unetched
4N5	15	900	13	~ 175
6N (99.9999%)	6	/	/	/
6N	10	/	/	~ 130
6N	16	900	13	~ 130

4.4   Aluminum cavities

In the following sections the focus is set to superconducting coaxial quarterwave resonators, in order to achieve high internal quality factors. Aluminum is a convincing choice, as the widely used metal is cheap in purchase and easy to process. Two sorts of aluminum, alloy 5083 (1N3) and high purity aluminum (5N), are used to fabricate the coaxial resonators. At first the machining process is kept identical with the one used for the copper cavities. After testing the set of cavities with the familiar inner and outer diameter choices $a = 2\,\text{mm}$ and $b = 5.25\,\text{mm}$, the machining process is altered including a new drill producing resonators of dimensions $a = 2\,\text{mm}$ and $b = 6\,\text{mm}$. This step aims to achieve the $3 : 1$ diameter ratio mentioned in section 3.1. Based on concerns of intense metal surface defects and impurities, the manufacturing process is further modified from drilling to sinker electrical discharge machining (SEDM). In addition the length of the waveguide section is prolonged to $L \geq 33\,\text{mm}$. The length of the stub is kept at $8\,\text{mm}$ for all cavity design versions. A picture of a cut, high purity aluminum coaxial resonator is shown in figure 4.5.

Figure 4.5: Picture of the etched high purity aluminum coaxial $\lambda/4$ resonator. After the measurements were finished, a vertical cut was carried out to make the inside of the cavity visible.

4.4.1   Surface preparation

To accomplish the optimum cavity performance a few hundred μm of the damaged surface layer get removed by chemical etching. This is realised with the commercially available phosphoric-nitric acid mix *Aluminum etch* by the company Alfa Aesar. A detailed description about the aluminum etch mechanism

and additional etch-rate measurements can be found in [10]. The chemical reaction equation follows [26]

$$7\mathrm{Al} + 5\mathrm{HNO_3} + 21\mathrm{H_3PO_4} \rightarrow 7\mathrm{Al(H_2PO_4)_3} + 13\mathrm{H_2O} + 2\mathrm{N_2} + \mathrm{NO_2} \qquad (4.14)$$

The nitric acid reacts with the aluminum, forming an aluminum oxide layer, which is dissolved by the phosphoric acid. If one visualizes the aluminum surface as peaks and valleys, the high viscosity of the etchant causes a flattening effect. Due to less agitation in the valleys, the etch solution locally becomes saturated and the reaction rate decreses. The etch rate is specified as $100\,\text{Å/s}$ at a temperature of $50°\,\text{C}$. To maintain the resonator's threads, which are for example used to mount SMA-connectors, stainless steel screws are attached before the cavity is placed in the acid bath. The etching procedure is carried out inside a flow box. To keep the temperature of the etch solution and furthermore the etch rate constant, the solution is preheated in a glass container on a hot plate and the temperature of the etchant is monitored with a digital thermometer. To prevent a saturated etch solution inside the cavity a magnetic stirrer is added to the glass container. Since the reaction is exotherm, it proved useful to preheat the etchant to $45°\,\text{C}$ and then turn off the hot plate. As the reaction is exotherm, the temperature will rise during the procedure. Cooling is realised by adding wet towels on the outer surface of the glass container. In order to avoid a saturated etchant, the acid bath is refreshed after two hours for another two hours. The total etching time of 4h should remove a $\sim 150\,\mu\text{m}$ layer off the surface. Afterwards the cavity is rinsed with distilled water, acetone and isopropanol inside an ultrasonic bath and blown dry with nitrogen. The removal of the resonator's surface layer is determined by measuring the outside dimensions of the resonator with a caliper rule before and after the etch treatment.

4.4.2   Results

The results of the measured quality factors of the superconducting aluminum resonators are summarized in table 4.2. Aluminum alloy 6061-T6 resonators yielded internal quality factors of about $Q_{\text{int}} = 0.3 \cdot 10^6$, either etched or unetched. The intrinsic metal impurities seem to determine the conductive losses, as the resonator's quality factor is unaffected by the surface etching treatment.

The internal quality factor of the first etched high purity aluminum resonator amounts to $Q_{\text{int}} = 1.5 \cdot 10^6$, which represents an improvement factor of roughly 2 caused by the etching process. A repeated quality factor measurement after 6

weeks mounted in the cold cryostat showed an identical result. A slight improvement of the modified diameter ratio $a : b = 3 : 1$ can be detected in measurements of the unetched cavities. After the etching treatment no remarkable difference can be detected. An explanation for this behaviour is the altered diameter ratio after the etching process.

The highest quality factor using the drill machining technique is achieved with a high purity aluminum resonator of the initial dimensions. After a surface removal of $\sim 200\mu$m the internal quality factor resulted in $Q_{\text{int}} = 5.6 \cdot 10^6$. Further 5h of etching yielded in $Q_{\text{int}} = 6.9 \cdot 10^6$. In this quality factor regime a noticeable power dependency is detected, which indicates saturable two level systems (TLS) [27], residing in an oxide layer on the metal surface. The unusual quality factor improvement for surface removals beyond $\sim 220\,\mu$m [8] lead to the implementation of a different machining process.

The SEDM technique is expected to interfere less strong with the aluminum surface layer. Furthermore the waveguide section of the resonator is prolonged and the diameter ratio optimized to reach $3 : 1$ after the etching process. The result is a cavity with a power dependent internal quality factor ranging from $11.3 \cdot 10^6$ at low input power levels to $13 \cdot 10^6$ at high input power levels. A plot of the obtained Q_{int} values as a function of the VNA output power and the estimated number of photons in the resonator is shown in figure 4.6.

Overall, the obtained internal quality factors are still an order of magnitude lower than expected. Reagor et al. reported intrinsic Q-factors ranging from $7 \cdot 10^7$ at the single photon level and $2 \cdot 10^8$ at large circulating field strengths with aluminum coaxial $\lambda/4$ resonators [7]. The faint trend of increasing Q_{int} suggests, that saturable two-level-systsem losses are not the main loss mechanism. It seems likely that the limiting factor is either conductor loss due to a finite surface resistance or a lossy dielectric layer on top of the metal surface. Further fine tuning of the machining and surface preparation process could lead to an improvement of the internal quality factors.

Table 4.2: Measured Q_{int} values of various aluminum coaxial quarterwave resonators at the cryostat's base temperature of about $20\,\text{mK}$ and VNA output power levels ranging from $-10\,\text{dBm}$ to $-90\,\text{dBm}$. The Q_{int} errors coming from the criclefit are not displayed, as they are in the range of $10^3 - 10^4$. A Q_{int} power dependence is detected for the resonators displayed in the last two rows of the table, where the low and the high input power value is given.

Purity	$Q_{\text{int}} \cdot 10^6$	Surface removal (μm)	Modifications	Machining
1N3	0.3	unetched	/	drilled
1N3	0.3	$\sim$300	/	drilled
5N	0.7	unetched	/	drilled
5N	0.9	unetched	$a:b \approx 3:1$	drilled
5N	1.5	$\sim$160	/	drilled
5N	1.6	$\sim$175	/	drilled
5N	1.7	$\sim$180	$a:b \approx 3:1$	drilled
5N	5.6	$\sim$200	/	drilled
5N	6.4-6.9	$\sim$450	/	drilled
5N	11.3 - 13	$\sim$150	$a:b \approx 3:1$, $L = 33\,\text{mm}$	SEDM
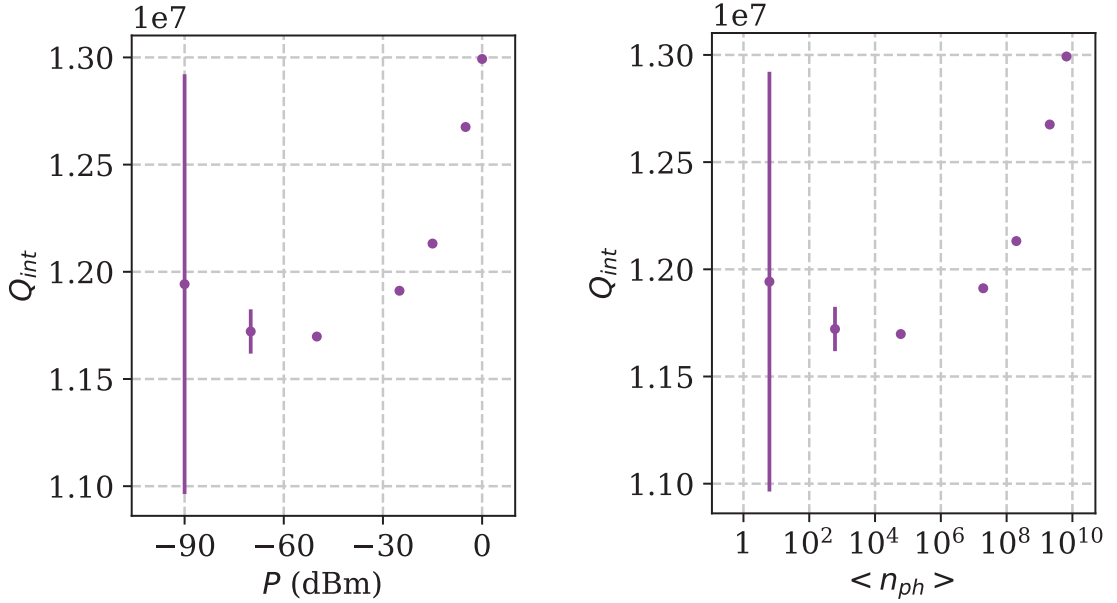
Figure 4.6: Q_{int} power dependence of the high purity aluminum coaxial quarterwave resonator. In the left plot the VNA output power is given in dBm, in the right plot the cavity input power is converted into an average inner cavity circulating photon number $\langle n_{ph} \rangle$.

Warm-up measurements

Beside the power dependence, the temperature dependence of the etched high purity aluminum coaxial resonator is investigated. Therefore the temperature of the resonator environment is stepwise raised up to 1.2K, using the cryostat's PID-controlled heaters. The measured resonator parameters Q_{int} and the resonance frequency change Δf_0 are shown in figure 4.7 as a function of the temperature. Approaching the critical temperature of aluminum $T_c = 1.19$K [20], the increasing surface resistance leads to a fall of Q_{int} and a shift in the resonance frequency [8]. The two fluid model considers the superconducting state by the presence of normal electrons of density n_n and superconducting electrons n_s. The sum of both densities form the conduction electrons n_c in the material. The normal electrons interact with the microwave field, which results in a finite surface resistance R_s. The surface resistance is solely affected by the normal electrons [28]

$$n_n = n_c \cdot \exp(-\frac{\Delta}{k_B T}) \tag{4.15}$$

where k_B depicts the Boltzmann constant and Δ the superconducting gap at zero temperature. The internal quality factor temperature dependence is then modelled by [29]

$$\frac{1}{Q_{\text{int}}^{R_s}} = \frac{A}{T} \cdot \exp(-\frac{\Delta}{k_B T}) + \frac{1}{Q_{other}} \tag{4.16}$$

The constant A covers the effective penetration depth, the normal state conductivity, the probe frequency and a further material independent constant. By adding an extra Q_{other}, temperature independent losses are included. The model is ed to match with the experimental data upon $T_c/2$. The internal quality factor data is approximated with a fit following equation 4.16. The fit parameters are $A = 1.1(2) \cdot 10^{-5}$ K and $Q_{other} = 1.43(4) \cdot 10^7$, indicating an overlying temperature independent loss mechanism. As expected, the fit function is in good agreement with the Q_{int} data until reaching roughly $T_c/2$. The measurement at the highest temperature of 1.2 K yields $Q_{\text{int}} \approx 10^4$, which represents the breakdown of superconductivity.
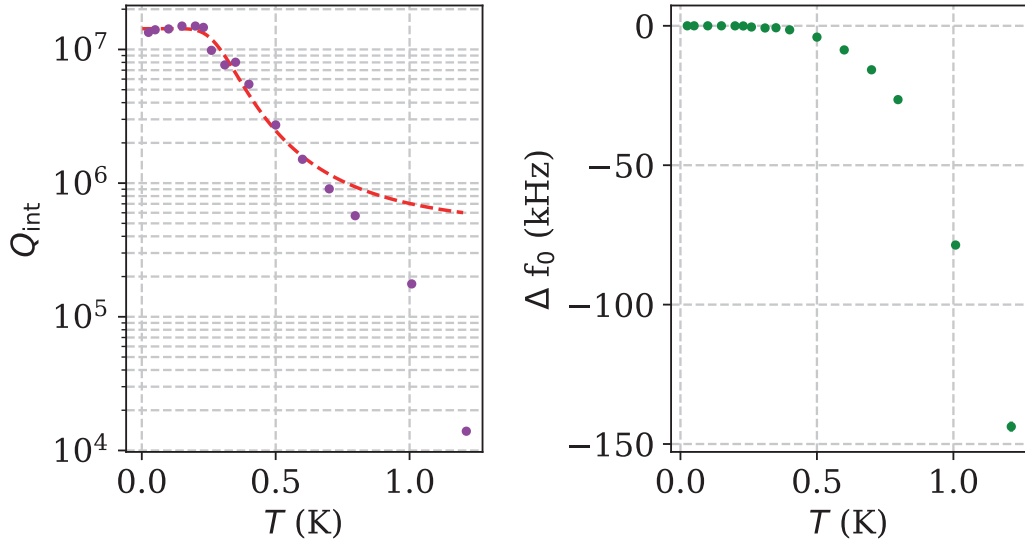
Figure 4.7: Warm up measurements up to $1.2\,\mathrm{K}$ using the cryostat's PID-controlled heaters. The temperature dependence of Q_{int} (left) and the resonance frequency change Δf_0 of the etched, high purity aluminum resonator are shown. Furthermore a fit function for the internal quality factor temperature dependence, considering a two fluid model, is displayed (dashed red line). The VNA output power is kept constant at $-65\,\mathrm{dBm}$ for each measurement.

4.5   Niobium cavity

Due to the high critical temperature $T_c = 9.2$K of niobium, it's availability in pure form and due to the thermal conductivity and machining characteristics it is the most common material choice for superconducting radiofrequency (SRF) accelerator cavities [30]. For this section, a coaxial quarterwave resonator is fabricated from high purity 3N5 niobium. It is machined using the sinker electrical discharge machining technique. The loss optimized resonator radii $a = 2.2$ mm and $b = 5.8$ mm are chosen to reach a $3 : 1$ ratio after a surface removal of $\sim 200\,\mu$m. The waveguide section amounts to $L = 36$ mm and the $\lambda/4$ stub is 8 mm. A picture of the niobium resonator is shown in figure 4.8. Typical

Figure 4.8: Picture of the high purity niobium coaxial quarterwave resonator, after the BCP surface treatment.

niobium SRF cavities operate at a resonance frequency of $f_0 = 1.3$ GHz and reach internal quality factors of $Q_{\text{int}} > 10^{10}$ at a temperature of $T = 1.5$ K and very high accelarating fields of several megavolts per meter [30]. These parameters are chosen to maximize the acceleration of the charged particle during the transit through the cavity. The high rf fields mount to $E_{\text{acc}} > 20$ MV/m, which corresponds to an average cavity population of about $\overline{n} = 10^{25}$ photons [31]. In comparison, aluminum coaxial quarterwave resonators used as quantum memory, in the field of circuit quantum elecdrodynamics (cQED), achieve internal quality factors of up to $Q_{\text{int}} = 7 \cdot 10^7$ at the average inner-cavity circulating power corresponding to a single photon [7]. The higher resonance frequency ranging typically from $4 - 12$ GHz, the lower temperature of about 30 mK and the much lower drive power make it more difficult for cQED cavities to deliver comparable high quality factors. Still, with reducing the dielectric loss at the cavity walls, a gain in Q_{int} is feasible.

The most common method to improve the niobium surface characteristics is

buffered chemical polishing (see section 4.5.1).

Coupling pin adjustment

In prospect of obtaining an internal quality factor in the range of $Q_{\text{int}} \approx 10^9$, the resonator's coupling pin and subsequently the coupling quality factor has to be adapted to achieve a sufficient S_{11} measurement. To receive a distinct S_{11} circle in the complex plain and therefore a reliable circle fit, the coupling quality factor has to be brought to approximately $Q_c \approx 10^8$. The diameter of the S_{11} circle in the complex plain and the dip depth of the signal's magnitude decrease with a growing Q_c compared to Q_l. By performing room temperature S_{11} measurements with a varying distance Δl between the coupling pin and the actual resonator, the exponential behaviour of Q_c can be determined, as displayed in figure 4.9. The results are in agreement with the simulated Q_c dependence in figure 3.5. Due to the low room temperature internal quality factor $Q_{\text{int}} \sim 10^3$ of the niobium cavity, the resonance is hardly detectable for coupling quality factors exceeding $\sim 10^6$. Utilizing a linear fit on a logarithmic scale, an estimation for the required coupling pin distance Δl is accomplished. As a result, Δl has to be adjusted to $\sim 4.1\,\text{mm}$ to achieve $Q_c = 1.2 \cdot 10^8$. This corresponds to a shortened coupling pin of about $\sim 5\,\text{mm}$. One has to keep in mind that the coupling into the cryostat and the thermal contraction of the coupling pin can lead to a further increase of Q_c. The measurements at base temperature reveal $Q_c = 2.4 \cdot 10^8$, which confirms the above considerations.
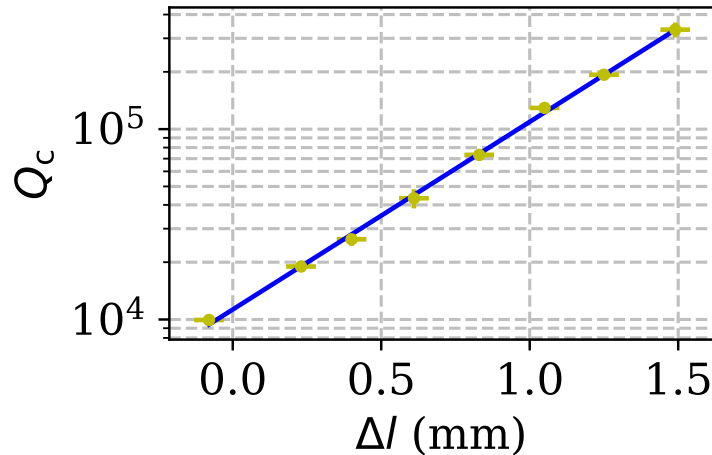
Figure 4.9: Niobium cavity room temperature Q_c measurements (yellow) with varying distance Δl between the coupling pin and the actual resonator. Furthermore a linear fit in the logarithmic scale is performed (blue) to demonstrate the exponential behaviour of Q_c.

4.5.1   Surface preparation

To optimize the niobium cavity surface characteristics, the well studied method of of buffered chemical polishing is used [32–35]. The chemical etching solution represents a mixture of hydrofluoric (HF), nitric (HNO_3) and phosphoric (H_3PO_4) acids. The main chemical reaction is given by [34]

$$6Nb + 10HNO_3 \rightarrow 3Nb_2O_5 + 10NO + 5H_2O \tag{4.17}$$

and

$$Nb_2O_5 + 10HF \rightarrow 2NbF_5 + 5H_2O \tag{4.18}$$
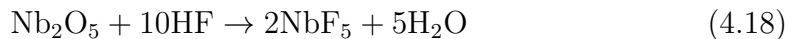
In the first step, the nitric acid oxidizes the niobium surface. Then, the hydrofluoric acid reduces the Nb_2O_5 into NbF_5, which represents a salt that gets dissolved in water. The addition of phosphoric acid acts as a buffer, that slows down the chemical reaction. The composition of the BCP mixture determines the etching characteristics and is mainly chosen to be either $1 : 1 : 1$ or $1 : 1 : 2$, which corresponds to the relative ratio of the components HF :HNO_3 : H_3PO_4.

As the procedure includes hydrofluoric acid, the task of the niobium coaxial $\lambda/4$ BCP surface preparation is handed to professionals at the university's institute for inorganic chemistry. To remove the top layer, which was exposed to the machining process, the resonator is placed into 555ml of an approximate $1 : 1 : 1$ BCP mixture inside a teflon container. To maintain a controllable etching process the container was surrounded by ice, as the etching rate strongly depends on the temperature [35]. This results in a BCP mixture temperature of roughly $0 - 5°\,C$. After 1h, phosphoric acid is added gradually in order to switch to the more moderate BCP composition of $1 : 1 : 2$. A magnetic stirrer is present during the whole process aiming for a steady flow of the BCP mixture. After the total treatment time of 2h, the niobium resonator is taken out and rinsed with deionised water and acetone. The total surface removal amounts to about $150\,\mu$m, quantified with a caliper rule considering the outer cavity dimensions.

4.5.2   Results

The internal quality factors of the niobium coaxial quarterwave resonator, measured at different VNA output power levels, are shown in figure 4.10. The cavity's Q_{int} ranges from roughly $0.5 \cdot 10^9$ at the single photon level to almost $1.2 \cdot 10^9$ at high cavity input power levels. For VNA output power levels below ~ -65dBm, or average photon numbers below $\sim 10^6$ respectively, Q_{int} stays constant. Above

that barrier, a rise in the internal quality factor is observed. The results, corresponding to photon lifetimes of $\tau_{int} = 10-24\,\mathrm{ms}$, demonstrate the highest internal quality factor yet reported for coaxial $\lambda/4$ resonators. The power dependent ascent of Q_{int} indicates, that the dominating loss mechanism is due to saturable two-level-systems [27], residing in the oxide layer of the niobium cavity.

A comparable result was reported recently from A. Romanenko et al., regarding niobium SRF cavities operating at $5\,\mathrm{GHz}$ and measured at $T = 20\,\mathrm{mK}$, that achieved interal quality factors $Q_{int} \geq 10^9$ at an average cavity population of about $\bar{n} \approx 10$ photons [36]. Their experiments with variant thickness of niobium oxide layers on the inner cavity surface demonstrate, that two-level-system (TLS) losses in the dielectric metal surface layer affect the internal quality factor. Additionally, their investigation on the effect of a $340°\,\mathrm{C}$ vacuum heat treatment, which modifies the Nb_2O_5 cavity surface layer, yields an internal Q increase of roughly factor 3. Applying the vacuum heat treatment on the coaxial $\lambda/4$ resonator, could lead to further Q_{int} improvement.
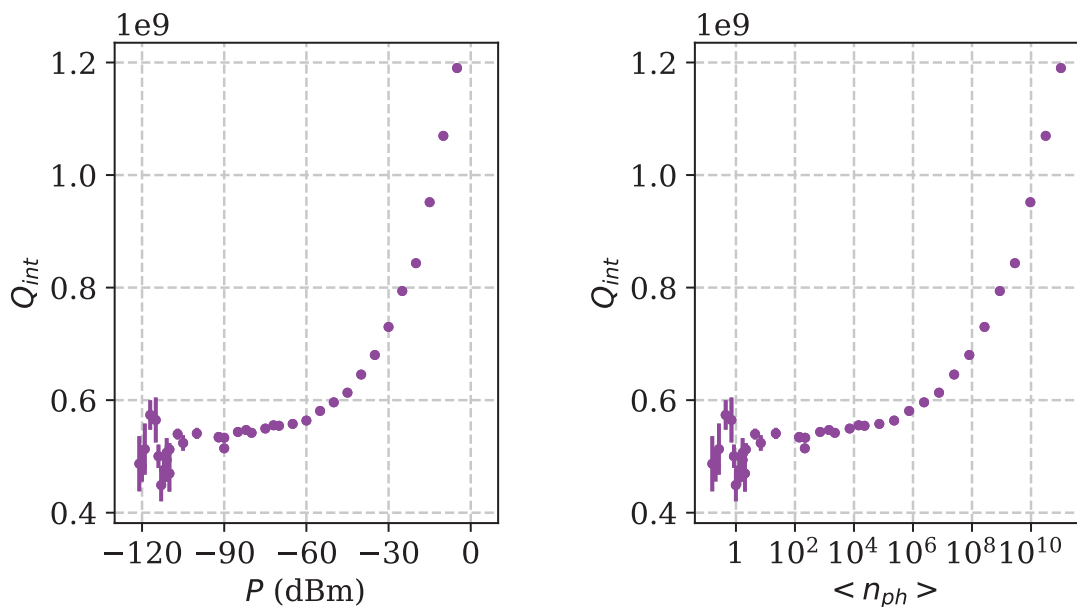
Figure 4.10: Q_{int} power dependence of the niobium coaxial quarterwave resonator. In the left plot the VNA output power is given in dBm, in the right plot the cavity input power is converted into an average inner cavity circulating photon number $\langle n_{ph} \rangle$.

Repeating the measurement of the niobium cavity after months of ageing, not preserved in a vacuum desiccator yields in a decreased Q_{int} ranging from $2.6 - 3.8 \cdot 10^8$, indicating a less pronounced power dependence. The results are shown in figure 4.11. A plausible explanation for the reduced internal quality

factor is the growth of an oxide surface layer, during the air exposed period. As a consequence, the enhanced dielectric loss of the resonator comes into effect.
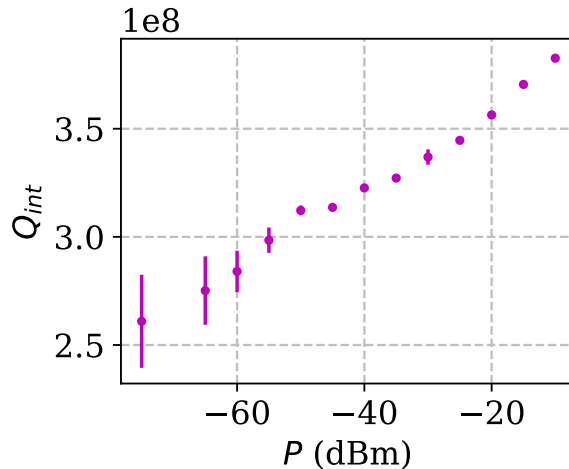
Figure 4.11: Q_{int} power dependence of the aged niobium coaxial quarterwave resonator as a function of the VNA output power.

Warm-up measurements

By raising the cryostat's temperature, using PID-controlled heaters, the temperature dependence of the niobium cavity parameters Q_{int} and Δf_0 are investigated. In two measurement cycles, stepwise warming up the cavity environment to $1\,\text{K}$ or $4\,\text{K}$, the internal quality factor and the shift of the resonance frequency get extracted. The VNA output power is set constant for each measurement to a value below the barrier of $-65\,\text{dBm}$, where the power dependency of the internal quality factor becomes apparent. The circlefit obtained resonator parameters are shown in figure 4.12 and 4.13.

Until approximately $1\,\text{K}$, an increase of Q_{int} occurs, starting from $0.5 \cdot 10^9$ and further exceeding 10^9. The internal quality factor rise, similar to the one seen in the power dependence (see 4.10), suggests TLS saturation due to thermal excitation [29]. According to [37], the internal quality factor in the TLS limited regime can be modelled by

$$\frac{1}{Q_{\text{int}}^{TLS}} = k \cdot \tanh\left(\frac{hf_0}{2k_B T}\right) + \frac{1}{Q_{other}} \tag{4.19}$$

with the combined loss parameter k, which includes the filling factor of the TLS host medium and the TLS dependent loss tangent at zero temperature.

Looking at the data of the $4\,\text{K}$ temperature range, the fall of Q_{int} and a shift

in the resonance frequency Δf_0 for temperatures above $1.4\,\text{K}$ can be detected. This effect can be explained by increasing conductive losses due to a growing surface resistance. Considering the two fluid model, as explained in the aluminum resonator warm up measurements of section 4.2, the Q_{int} temperature dependence follows equation 4.16. Since the breakdown of superconductivity occurs at the critical temperature of $T_c = 9.2\,\text{K}$, Q_{int} reaches at 4K still a value in the range of 10^6. By combining the two temperature dependent Q_{int} models considering TLS and conductive losses, as its done in [29], a fit function with the parameters A, k and a combined Q_{other} is derived

$$\frac{1}{Q_{\text{int}}^{TLS+R_s}} = k \cdot \tanh\left(\frac{hf_0}{2k_BT}\right) + \frac{A}{T}\exp\left(-\frac{\Delta}{k_BT}\right) + \frac{1}{Q_{other}} \tag{4.20}$$

The fit result with the parameters $A = 2.3(1) \cdot 10^{-5}\,\text{K}$, $k = 1.9(9) \cdot 10^{-9}$ and $Q_{other} = 9.7(3) \cdot 10^9$ is shown in figure 4.12. The measured internal quality factors follow the theoretical predictions. The slight deviation at higher temperatures could originate from incomplete thermalisation.
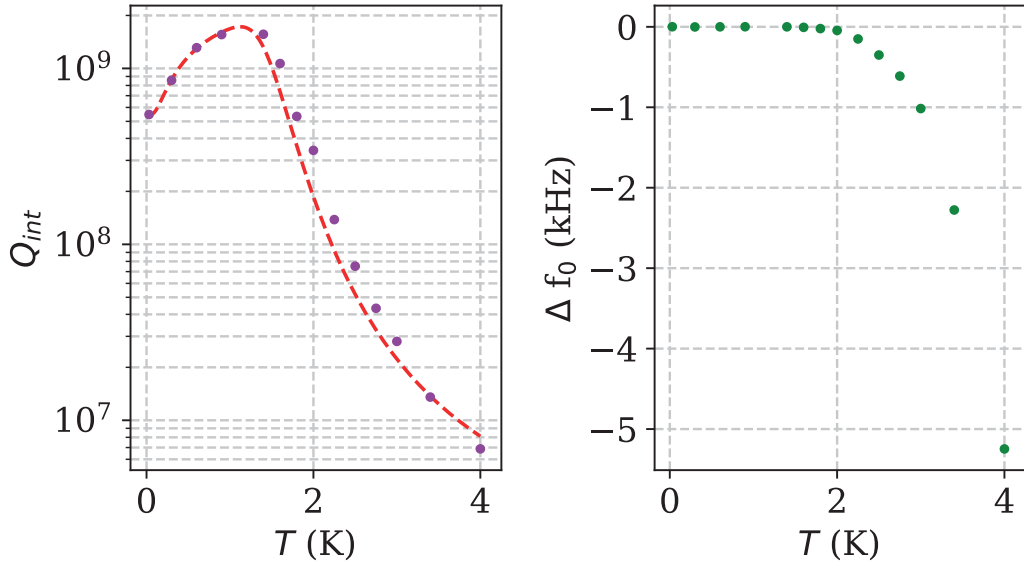
Figure 4.12: First series of warm up measurements up to $4\,\text{K}$ using the cryostat's PID-controlled heaters. The niobium resonator temperature dependence of Q_{int} (left) and the resonance frequency change Δf_0 (right) are displayed. Furthermore a fit function (dashed red line) for the internal quality factor temperature dependence considering TLS and conductor losses is shown. The VNA output power is set to $-75\,\text{dBm}$ for each measurement.

The second warm up measurement series focuses on temperatures up to 1K, where the resonator is likely to be limited to TLS energy dissipation. The gain

in Q_{int}, while increasing the temperature, is shown in the top panel of figure 4.13, including a fit in the form of equation 4.19 regarding solely thermal TLS saturation. The fit parameters are $k = 1.62(3) \cdot 10^{-9}$, and $Q_{other} = 4.4(4) \cdot 10^9$. Compared to the TLS limited regime in the warm up measurement up to 4K, the Q_{int} values reach slightly higher values, which can explain the different fit parameters for the combined loss parameter k. A reason could be a mild ageing effect, as the 4K warm up cycle was performed weeks after the 1K warm up measurement series. The roughly factor 2 difference of the fitted value for the temperature independent loss mechanism Q_{other} seems to be a consequence of the disregarded conductive losses in the exclusive TLS fit model. To perform the combined fit model, more measurement points in the higher temperature range would be needed.

TLS possess an electric dipole moment, which couples to the electric field of the resonator. The resonant interaction leads to change of the dielectric constant, when the temperature is varied, which results in a small, anomalous frequency shift [27] following

$$\Delta f_0^{TLS}(T) = f_0 \frac{k}{\pi} \cdot \left(\text{Re} \Psi \left(\frac{1}{2} + \frac{1}{2\pi j} \frac{hf_0}{k_B T} \right) - \log \left(\frac{1}{2\pi} \frac{hf_0}{k_B T} \right) \right) \tag{4.21}$$

with the complex digamma function Ψ and the imaginary unit j. As the resonance frequency change is in the range of a few Hz, the contribution of the resonator's stub thermal expansion, which leads to a decreasing resonance frequency while warming up, is included to the model. To estimate the additional frequency shifting effect the following approximation is done: the $\lambda/4$ stub's linear thermal expansion is given by

$$\frac{\Delta l'}{l'} = \alpha \Delta T \tag{4.22}$$

with the linear thermal expansion coefficient α, the cavity's stub length l', it's length change l' and the change in temperature ΔT. Assuming the variation of the resonant wavelength is only affected by the stub's expansion yields

$$\Delta \lambda_0 = 4\alpha \Delta T l' \tag{4.23}$$

and

$$\Delta f_0 = \frac{c}{\lambda_0} \frac{\Delta \lambda_0}{\lambda_0} \tag{4.24}$$

for $\Delta \lambda \ll \lambda$. Summarizing the considerations, the equation describing the total

temperature dependent frequency shift is given by

$$\Delta f_0(T) = \Delta f_0^{TLS}(T) - f_0 \cdot 4l' \Delta T \, \alpha \, \frac{f_0}{c} \qquad (4.25)$$

The result of fitting equation 4.25 to the frequency shift data obtained from the warm up measurements is displayed in the bottom panel of figure 4.13. It is assumed that the stub's length amounts to $l' = 8\,\mathrm{mm}$ at zero temperature. Furthermore a constant offset is added to the fit formula. The fitted values for the combined loss parameter and the linear thermal expansion coefficient are $k = 3.2(4) \cdot 10^{-9}$ and $\alpha = 1.1(2) \cdot 10^{-9}\,\mathrm{K}^{-1}$. The higher value of the fitted combined loss parameter k, compared to the k's obtained from previous Q_{int} temperature analysis, can be explained with the contribution from off resonant TLS excitations to the frequency shift [37]. Another explanation could be the insufficiency of the linear approximation of the stub's length thermal expansion. A literature value of the niobium linear expansion coefficient $\alpha = 3 \cdot 10^{-9}\,\mathrm{K}^{-1}$ at a higher temperature of $T = 6\,\mathrm{K}$ is found in [38], which is in the same order of magnitude as the fit obtained value.
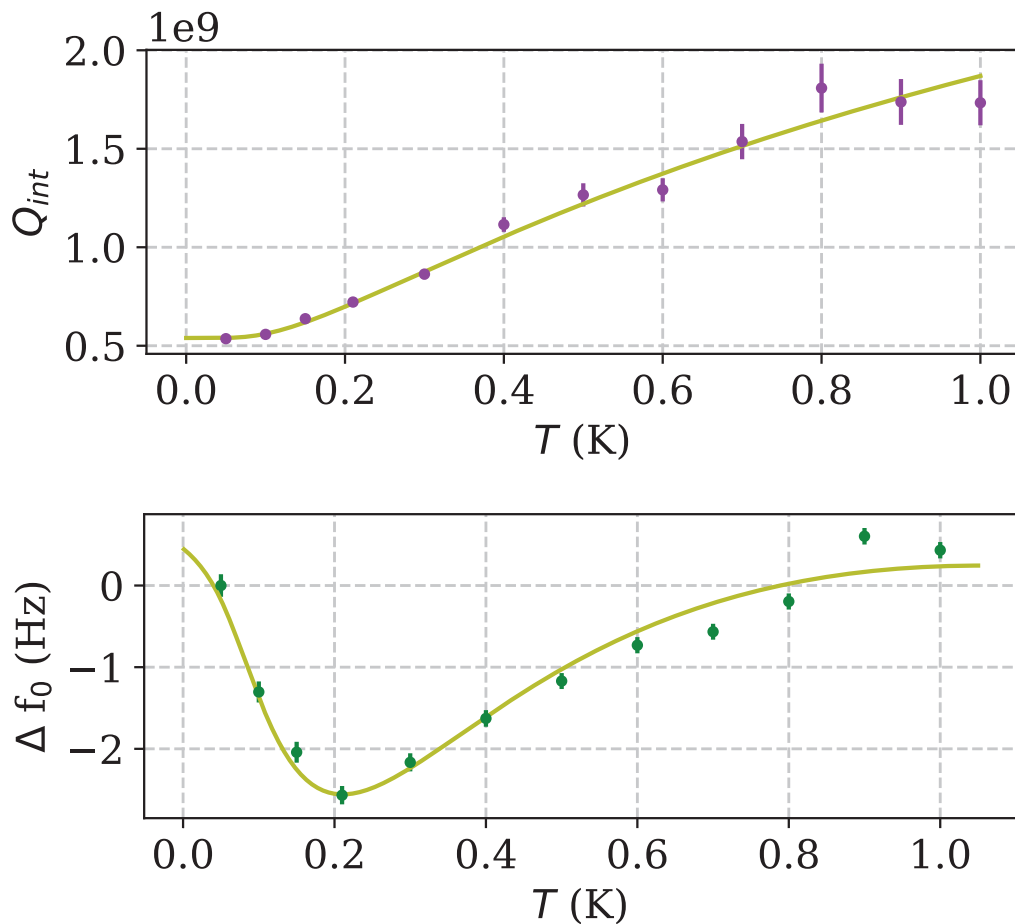
Figure 4.13: Second warm up measurement series up to $1\,\mathrm{K}$ of the niobium cavity. The temperature dependent change of Q_{int} (upper plot) and the variation of the resonance frequency Δf_0 (bottom plot) is shown. The solid yellow lines represent fit functions concerning thermal two level system excitation. For the resonance frequency change the additional effect of the thermal expansion of the resonator's stub is added to the fit model. The VNA output power is set to $-100\,\mathrm{dBm}$ for each measurement, which corresponds to roughly ~ 10 photons circulating in the resonator.

4.6   Summary

The high-Q coaxial $\lambda/4$ microwave resonator is fabricated from copper, aluminum and niobium. The copper cavities reach the lowest internal quality factors, as the magnetic participation ratio of the resonator design is not ideal for normal conducting metals. Both, etching with cupric chloride and annealing in the presence of reduced oxide pressure improved the cavity's internal quality factor to values in the range of $\sim 10^4$.

The aluminum cavities show higher internal quality factors exceeding a million, after a surface removal of more than $150\,\mu$m. A change in the machining method and modified cavity design parameters, including a higher waveguide section and a loss optimized diameter ratio, leads to a quality factor of $Q_{\mathrm{int}} = 1.3 \cdot 10^7$. A slight Q_{int} power dependence indicates the presence of saturable two-level-systems on the cavity surface, but the main loss mechanism seems to be either conductor loss due to a finite surface resistance or a lossy, non saturable dielectric layer on top of the inner cavity walls. The warm up measurements until the breakdown of superconductivity at $1.2\,$K show a shift of the resonance frequency and a decrease of the internal quality factor due to an increasing surface resistance. A fit considering the two fluid model agrees well with the Q_{int} data until $T_c/2$.

The niobium cavity achieves quality factors of $Q_{\mathrm{int}} = 1.2 \cdot 10^9$ in the high input power regime and $Q_{\mathrm{int}} = 0.5 \cdot 10^9$ at the single photon level, after the BCP surface treatment. The Q_{int} increase with rising temperature until roughly $1\,$K and the pronounced Q_{int} power dependence indicate saturable two-level-systems (TLS) in the niobium oxide layer as the limiting factor. A fit, considering the conductive and the TLS losses, is in agreement with the data in the warm up temperature range, which ends at $4\,$K. By investigating the resonance frequency shift in the TLS loss dominated temperature range until $1\,$K, an additional frequency shifting effect due to the resonator's stub thermal expansion emerges. From a fit, considering the TLS and the stub's length induced shift of frequency, the thermal linear expansion coefficient $\alpha = 1.1(2) \cdot 10^{-9}\,\mathrm{K}^{-1}$ is extracted.

5   Time domain measurements

5.1   Introduction

In addition to evaluating the behaviour of a resonator in the frequency domain, there is also the possibility to gain information about the cavity's performance by measuring in the time domain. This approach is prevalent in the field of high-energy particle physics to obtain the internal quality factor Q_{int} of superconducting radiofrequency (SRF) accelerator cavities. The knowledge of Q_{int} is mandatory to evaluate the benefits of different surface treatments or cavity geometries. Typical niobium SRF cavities achieve internal quality factors of $Q_{\text{int}} > 10^{10}$ [30]. Assuming to be in the critically coupled regime, the very sharp resonance of $\Delta f = 0.26\,\text{Hz}$ would turn a frequency domain measurement with a network analyzer, aiming to extract Q_{int}, into a challenging up to impossible task.

In this chapter, the timedomain measurements of a niobium coaxial quarterwave resonator are discussed. A part of the data analysis is based on standard SRF measurement techniques. A more detailed description can be found in [30], chapter 8. A numerical fit routine is used to extract the loaded quality factor Q_{l} from the power decay of the cavity. The results are used to obtain the coupling and internal quality factors and compared with previous frequency domain measurements of the same cavity. Furthermore, a formula for the transient cavity behaviour of the reflected power, including the possibility of a detuning in the cavity input signal, is derived.

5.2   Overview, Setup and Example Measurement

5.2.1   Overview

The standard SRF measurement techniques concentrate on measuring the cavity response to radio frequency (rf) fields. Therefore, the exponential decay of the stored energy, after switching off the resonant rf source is recorded. The time profile of the power P(t) leaking out of a cavity, after turning off the rf drive at t = 0 follows

$$P(t) = P(0) \cdot e^{-t/\tau} \tag{5.1}$$

where τ describes the decay time constant. Knowing the cavity's resonance frequency f_0, the loaded quality factor can be calculated with $Q_{\text{l}} = 2\pi f_0 \tau$.

Once Q_l is known, the next step is to obtain the coupling and the internal quality factors Q_c and Q_{int}. For this purpose the transient behaviour of the cavity is examined by acquiring the reflected power signal, while switching on the cavity drive. One method is to obtain the coupling strength

$$\beta = \frac{Q_{int}}{Q_c} \tag{5.2}$$

by measuring the power levels P_f and P_r of the cavity response directly after switching the resonant rf source on and after reaching steady state. The ratio of these power levels leads to the coupling strength via

$$\beta = \frac{1 \pm \sqrt{P_r/P_f}}{1 \mp \sqrt{P_r/P_f}} \tag{5.3}$$

for the cavity being overcoupled $\beta > 1$ (upper sign) or undercoupled $\beta < 1$ (lower sign). The coupling strength determines the strength of the interaction between cavity and coupler. In the overcoupled case, the main loss channel is due to power leaking out via the coupler. In the undercoupled case, the power dissipation in the cavity walls is dominating. The shape of the cavity response to a resonant rectangular drive pulse allows the distinction between the over- and undercoupled case, as depicted in figure 5.1.

Knowing β and Q_l, the internal quality factor follows

$$Q_{int} = Q_l (\beta + 1) \tag{5.4}$$

By modelling the resonator with an equivalent circuit and using energy conservation relations on resonance, an equation for the reflected power

$$P_r(t) = P_f \left\{ 1 - \frac{2\beta}{1+\beta} \left[1 - \exp\left(-\frac{t}{2\tau}\right) \right] \right\}^2 \tag{5.5}$$

describing solely the cavity ring up, can be derived [30]. For $\beta > 1$, the equilibrium power level of $P_r(t)$ is reached after passing the zero power line. Since equation 5.5 is only valid on resonance, the task to find an expression, that allows small detuning δ of the cavity drive, is completed with the useful tool of Laplace- and inverse Laplace-transform (see section 5.7). The rather bulky equation 5.6, describing the transient behaviour of the resonator with the drive switched on at $t = 0$, is expressed in terms of Q_{int} and Q_c, instead of β and τ.
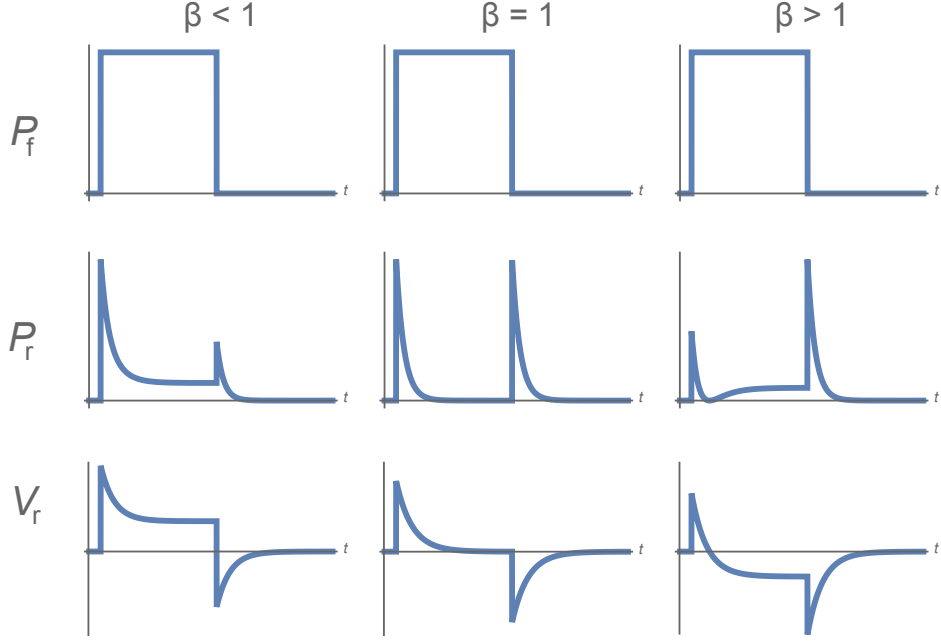
Figure 5.1: Schematic cavity response to a resonant rectangular powerpulse P_f in the under-, critically and overcoupled regime. P_r is the reflected power signal and V_r the reflected wave amplitude. Adapted from [30], figure 8.5.

$$P_r(t) = \frac{P_f}{4Q_c\delta^2 Q_i^2 f_0^2(Q_c + Q_i)^2}\Big[4Q_c^2\delta^2 Q_i^2 + f_0^2(Q_c - Q_i)^2 +$$
$$4Q_i^2 f_0^2 exp(-\frac{2\pi f_0(Q_c + Q_i)t}{Q_c Q_i}) + 4Q_i f_0 exp(-\frac{\pi f_0(Q_c + Q_i)t}{Q_c Q_i})$$
$$\cdot\Big(f_0(Q_c - Q_i)\cos(2\pi\delta t) - 2Q_c\delta Q_i\sin(2\pi\delta t)\Big)\Big] \quad (5.6)$$

For zero detuning $\delta = 0$, equation 5.6 corresponds to equation 5.5. The effect of driving the cavity slightly off resonant is shown in figure 5.2. The minimum in the reflected power of a cavity in the overcoupled regime ($Q_{int} > Q_c$) shortly after switching on the cavity drive, does not meet the zero power line for $\delta > 0$.

5.2.2 Setup

To measure the niobium coaxial quarterwave resonator in the time domain the following device-setup is used: a rf-signal generator provides an input pulse at the cavity's resonance frequency, which is obtained from preceding VNA measurements. To make sure to reach the steady state, the length of the pulse is chosen to be roughly ten times the cavity lifetime τ. The resonators field build-
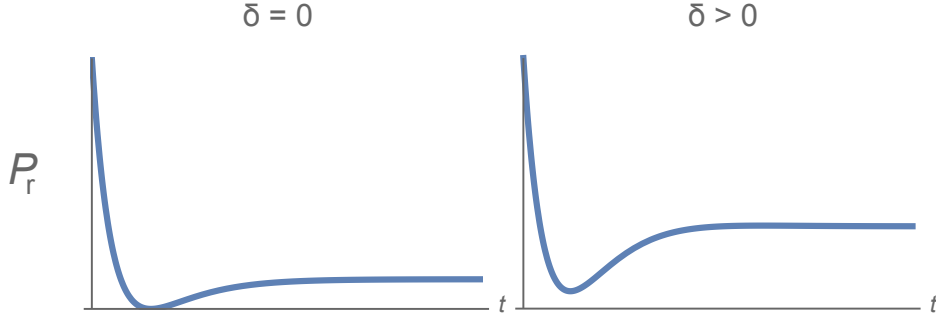
Figure 5.2: Transient cavity behaviour after switching on a resonant (left) or slightly detuned (right) rf drive. P_r describes the cavity's reflected power, δ the detuning between the rf drive and the resonance frequency. Except δ, all other parameters are identical in both cases and $\beta > 1$.

up, while applying the pulse, and the cavity decay towards the pulse get recorded with a spectrum analyzer. More precisely, the reflected power signal of the cavity is measured in the time domain. The input signal generator and the spectrum analyzer are connected to a function generator, which synchronizes both devices. In this way, averaging of the data traces for each input power can be realised, in order to improve the signal to noise ratio. The experimental setup inside the cryostat is equal to the setup used prior to measure the niobium cavity in the frequency domain (see section 4.1).

5.2.3 Example Measurements

Figure 5.3 displays the distinct shape of the cavity response to a resonant drive pulse starting at $t = 0\,\text{s}$ and ending at $t = 0.04\,\text{s}$ for various drive powers. The sampling rate and the number of samples of the spectrum analyzer are kept constant for each measurement. The averaging factor ranges from 50, for the highest input power, to 2000 for the lowest input power. The choice of measurement parameters is made considering measurement duration and signal-to-noise-ratio.

In figure 5.4 a single, high power measurement of the cavity response to a rf drive pulse is shown. Comparing the shape of the cavity response to figure 5.1 allows the assumption, that the resonator-transmission line system is in the overcoupled regime ($\beta > 1$). The fact, that the minimum, shortly after switching on the rf drive, is not arriving down at the noise floor, already indicates a small detuning. This detail can be seen in the logarithmic plot of the reflected power in figure 5.4.

One can classify three stages, the resonator goes through in each measurement
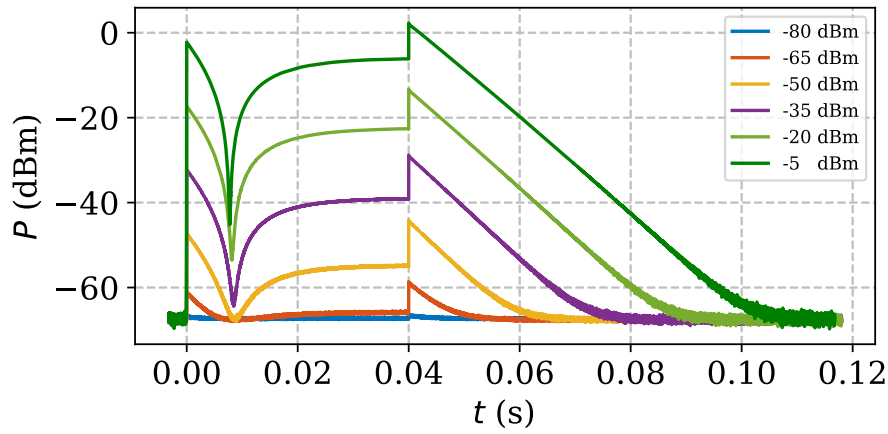
Figure 5.3: Datatraces of the reflected power signal for different cavity input pulse power levels in logarithmic scale. Therefore, the rf drive output power was modified from –5dBm (top trace) to -80dBm (bottom trace), where the signal vanishes in the noise floor.
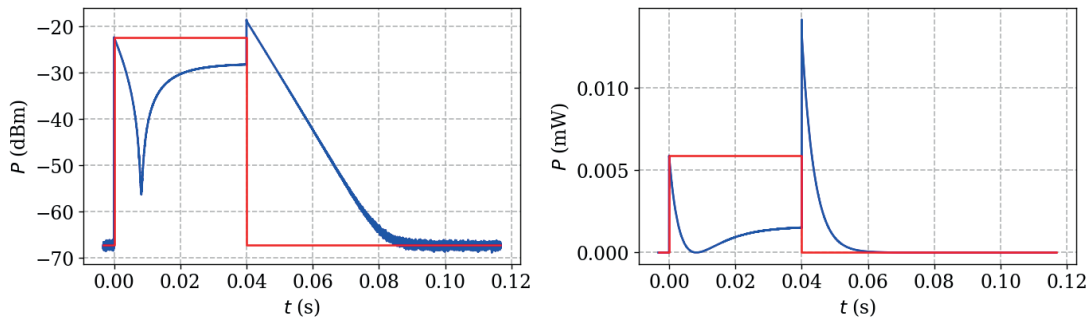
Figure 5.4: Raw data trace of the niobium coaxial quarterwave resonator measured in reflection in the time domain (blue) and a schematic drive pulse sequence (red). The reflected power is plotted in logarithmic (left) and linear scale (right). The rf drive output is set to $-25\,$dBm.

48

cycle, which are illustrated in figure 5.5. The Cavity ring-up starts when the
drive pulse is switched on. At this point the cavity is empty and starts to fill. A
part of the travelling signal enters the cavity, builds up the field in the resonant
mode and is reflected back with a phase shift. The other part of the signal gets
reflected directly at the coupler. The reverse travelling signal consists of the sum
of two out of phase signals. As the energy stored in the cavity rises, the cavity
emitted signal cancels an increasing part of the directly reflected signal. At the
dip in the reflected power, both signal parts have equal amplitudes. Then, the
cavity emitted signal starts to dominate over the directly reflected signal. As a
consequence, the total reverse travelling signal becomes π phase shifted (see time
profile of V_r in figure 5.1). Since the power measurement is phase insensitive,
the reflected power rises after the dip until an equilibrium is reached. In the so
called steady state the stored energy of the cavity is constant. When the drive
is abruptly turned off, the part of the signal, which gets reflected directly at the
coupler, disappears. Due to the absence of one part of the two competing signals,
a sudden jump in the reflected power emerges. This is followed by an exponential
fall of the reflected power, as the stored energy of the undriven cavity starts to
decay until it is empty.
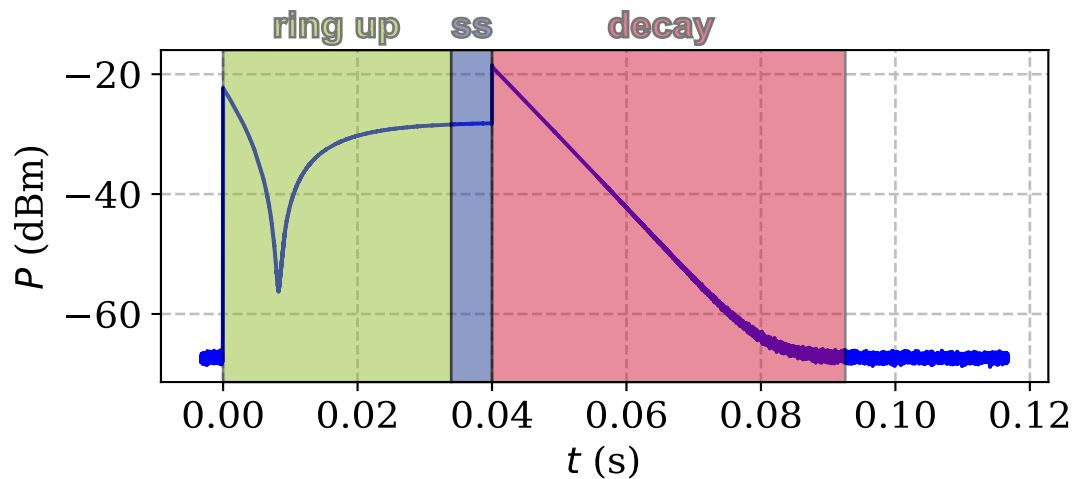
Figure 5.5: Characterisation of three stages the cavity undergoes during each
pulse sequence: ring up, steady state (ss) and decay. The reflected power is
plotted in logarithmic scale. The rf drive output is set to $-25\,\mathrm{dBm}$.

5.3   A closer look at the decay

The main idea evaluating the cavity decay data is to extract the lifetime of the cavity and hence the loaded quality factor. After turning off the rf drive, the total lost power P_{tot} is equivalent to the power leaking out the coupler P_{e} and the power dissipated in the cavity walls P_{c}.

$$P_{\text{tot}} = P_{\text{c}} + P_{\text{e}} \tag{5.7}$$

With the definition of the loaded quality factor

$$Q_{\text{l}} = \frac{\omega_0 U}{P_{\text{tot}}} \tag{5.8}$$

where ω_0 is the angular resonance frequency and U is the stored energy of the resonator, a differential equation for the decay can be set up.

$$\frac{dU}{dt} = -P_{\text{tot}} = \frac{\omega_0 U}{Q_{\text{l}}} \tag{5.9}$$

A solution to this equation is

$$U(t) = U_0 \, \exp\left(-\frac{\omega_0 t}{Q_{\text{l}}}\right) \tag{5.10}$$

where U_0 defines the energy at $t = 0$. According to that, the expression for the reverse travelling power is

$$P(t) = P_0 \, \exp\left(-\frac{\omega_0 t}{Q_{\text{l}}}\right) \tag{5.11}$$

In terms of this result, a linear fit of the reflected power signal in the logarithmic scale leads to the loaded quality factor. But this has to be used with caution, since equation 5.11 is only valid as long as Q_{int} and as a consequence Q_{l} remains constant during the decay. If Q_{int} is power dependent and changes, while the stored energy in the cavity decreases as the input drive is shut off, the power decay cannot be described by a simple exponential anymore. One option to circumvent this problem is to implement a numerical fit, where the decay data is divided into sections. Instead of one loaded quality factor for the whole decay, Q_{l} is obtained for each section, following the change of Q_{int}.

5.4   Noise floor subtraction

A crucial point in the analysis of the reflected power data is the noise power subtraction. The impact of the added noise floor gets visible especially in the logarithmic scale, which is shown in figure 5.6, where the noise floor lifts the tail of the power decay trace. This effect distorts the linear fit results at low power levels to obtain the loaded quality factor. The level of the noise floor is obtained by averaging over reflected power data without an input power applied. The determination of the noise floor and the subtraction are made in the linear power scale. This is done for every reflected power trace ahead of any further analysis.
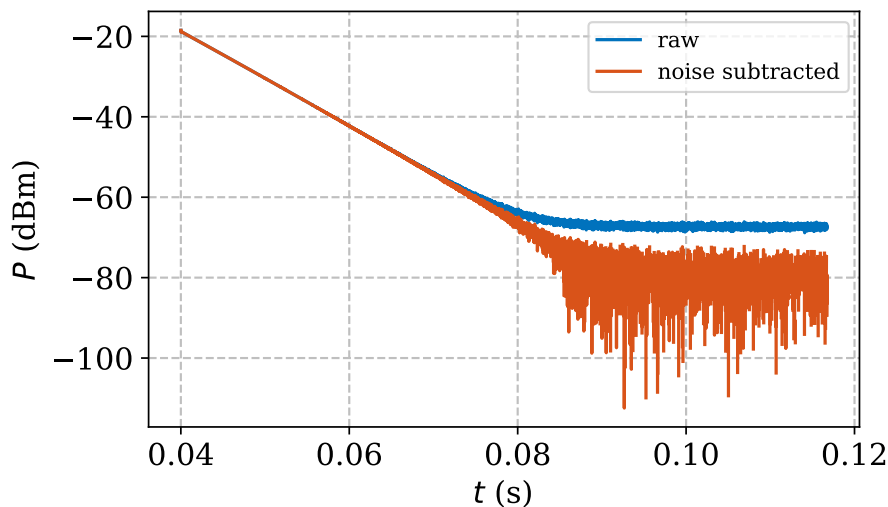
Figure 5.6:   Comparison of a powerdecay trace at a cavity drive power of $-25\,\mathrm{dBm}$ in the logarithmic scale with (red) and without (blue) noise floor subtraction.

5.5   Numerical fit routine

The power decay data is fitted with a numerical fit model, since the decay characteristic is not solely exponential and therefore cannot be fitted with a single linear fit in the logarithmic scale. Each decay trace is split into minor slices and for every slice a linear fit is performed. From the slope of each fit Q_l is extracted and connected to the slice's mean power value. The full python code of the fit routine is shown in appendix 1.

The first peak of the decay is scaled to the rf drive power output, in order to make the outcome comparable to VNA measurements in the frequency domain. The result is not only one single Q_l value for each input drive pulse, but an extended trace of Q_l values depending on the decreasing power leaking out of

the cavity after switching off the drive. This displays the big advantage of the numerical decay fit, since the usual input power sweep method, to obtain a power dependence of the quality factor, requires a measurement for each input power value. The outcome of the numerical fit routine for each input drive pulse is shown in figure 5.7. Additionally plotted are Q_l values of the same cavity, but obtained from VNA frequency domain measurements using the circlefit.

The first Q_l values of the numerical fits at the high power end of each trace are in agreement with the Q_l values from the circlefit data. The Q_l traces starting below $-60\,\mathrm{dBm}$ match with the reference Q_l values, but contain high fluctuations due to higher noise levels at low power. Following the traces starting above $-60\,\mathrm{dBm}$, a gap between the reference circlefit Q_l values and the numerical Q_l fit traces emerges. At the low power end of these traces, the numerical Q_l values are systematically above the reference Q_l values. This reveals that after switching off the drive, the stored energy in the cavity leaks out slower, which yields in higher Q_l values as expected from the circlefit data. This behaviour could be explained with long-lived two level systems (TLS) on the cavity surface, which are saturated, when the cavity is in steady state, but absorb energy leaking out of the cavity after turning off the drive. Quasi particle recombination could as well be responsible for the enhanced lifetime of the decaying resonator mode.

Another explanation would be a coupling strength dependent initial power P_0 in equation 5.11. In this regard, a more accurate expression for the power decay is necessary. By Laplace-transforming the product of a rectangular function with a cavity resonant oscillation and inverse Laplace-transforming the outcome multiplied with a matching transfer function, an analytical formula for the cavity ring up and decay can be found. This procedure is explained in detail in section 5.7. The anticipated result,

$$P_r(t) = P_f \frac{4\beta^2}{(1+\beta)^2} \, \exp\left(-\frac{\omega_0 t}{Q_l}\right) \tag{5.12}$$

describes the reflected power of the cavity decay for the resonator beeing in the steady state right before the drive switch-off at $t = 0$, with the cavity forwarded drive power P_f. This is consistent with [30], where the same formula is derived via energy conserving relations on resonance. An altering β, corresponding to the falling power during the decay, could explain the upwards bent Q_l traces. The values of the decaying power in the numerical fit are scaled to the input drive at the very beginning of the decay, where β is at it's peak value. In other words, the power levels, the numerical fitted Q_l values are connected to, would need a β
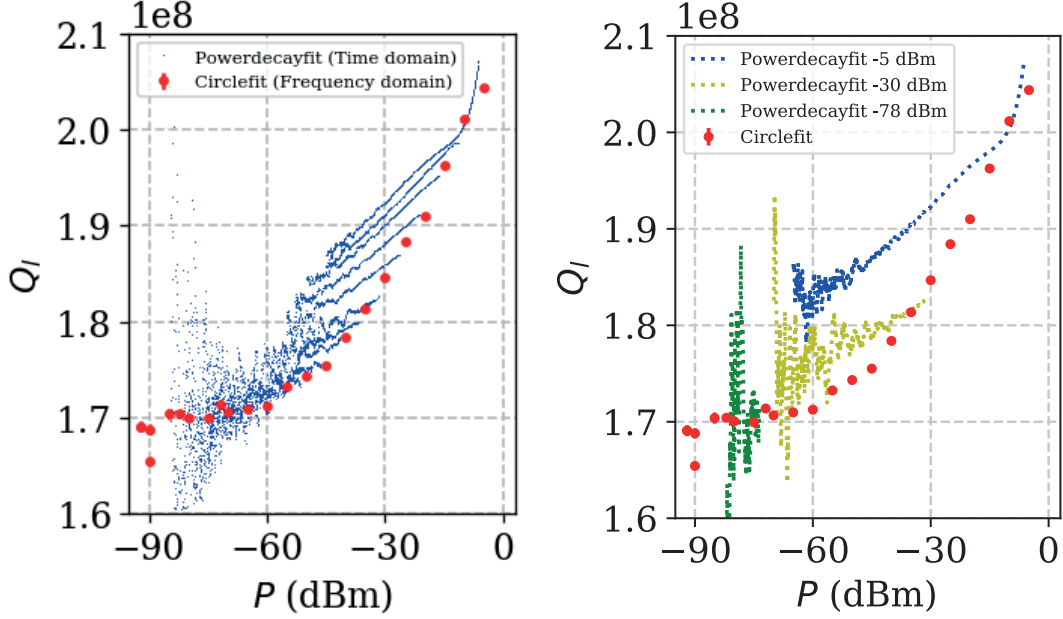
Figure 5.7: Power dependend Q_l traces for different input pulse power levels as a result of the numerical power decay fit compared to Q_l data (red) extracted from scatteringparameter measurements in the frequency domain using the Circlefit. **left plot:** the Q_l traces of all input pulse power levels are displayed. Each blue dot represents a numerical fitted Q_l value, depending on the powerlevel leaking out the cavity. **right plot:** a selection of Q_l traces for three input pulse power levels, covering the entire input power range, is shown.

dependent rescaling. But in this case, where β values range from approximately 5 at high power to 2 at low power levels, it would be a minor effect in the opposite direction. A decreased coupling strength leads to a lower prefactor in the calculation of the power value, to which Q_l is linked, and therfore to an even larger distance between timedomain and VNA data.

The diverging Q_l decay traces in the high power regime imply a weak spot of the numerical fit routine. Nevertheless, the Q_l values obtained from the highest power slice of each trace at early times of the decay, where the variation of β is insignificant, are shown in figure 5.8. The results agree well with the Q_l power dependence measured in the frequency domain, decreasing from $Q_l \sim 2 \cdot 10^8$ at high input fields to a constant plateau of $Q_l \sim 1.7 \cdot 10^8$. At low input power levels the uncertainty of the fitted decay constant grows due to higher measurement noise, which can be observed in the rising errorbars of Q_l. These results are further used to extract the internal and coupling quality factors.
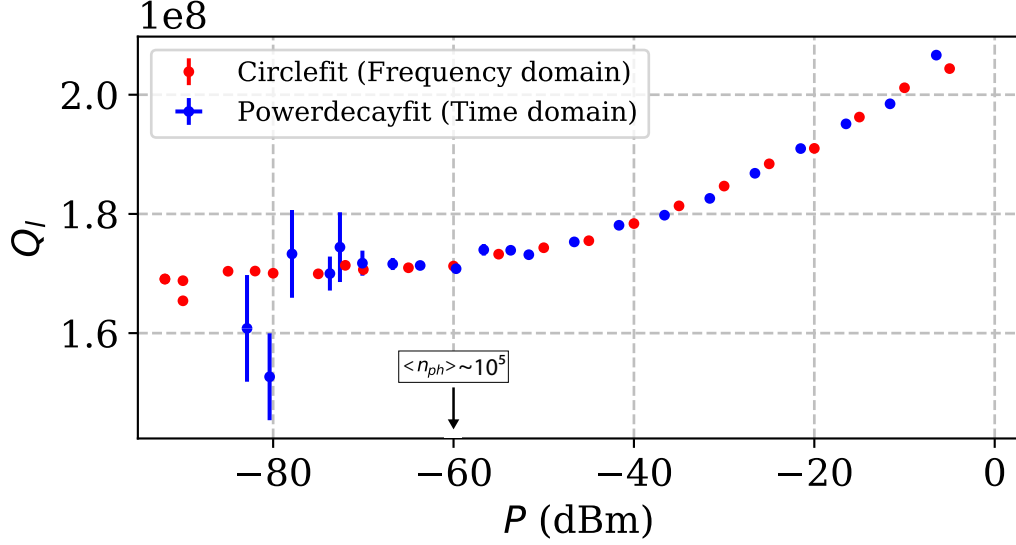
Figure 5.8: Extracted Q_l values from the first slice of the numerical power decay fit (blue) and from scattering parameter measurements in the frequency domain using the circlefit (red).

5.6 Determining internal and coupling Q

An example demonstrating the link between measurements in the time and frequency domain is shown in figure 5.9. In the frequency domain, the dip depth of the normalized scattering parameter reflection coeffiecient on resonance is determined by

$$|S_{11}| = |\,2Q_\mathrm{l}/Q_\mathrm{c} - 1\,|$$
(5.13)

In the time domain measurement, the reflected power aims for a constant value P_r, considering the resonant power pulse to be long enough. In a S_{11} measurement, one acquires the ratio of cavity output to input signal, while sweeping the frequency. Far off resonance, the travelling signal cannot enter the cavity and the input signal gets fully reflected. Its equivalent in the time domain measurement is the peak of the reflected power P_f, directly after switching on the drive. The ratio of the resonant and off resonant $|S_{11}|$ magnitude resembles the reflected power value ratio P_r to P_f. The only difference is that the scattering parameter measurement gathers the ratio of voltage signals. This can be solved with squaring or taking the square root respectively. The expression

$$\frac{P_\mathrm{r}}{P_\mathrm{f}} = (2Q_\mathrm{l}/Q_\mathrm{c} - 1)^2$$
(5.14)

concludes the precedent considerations. One can arrive at the very same result

54
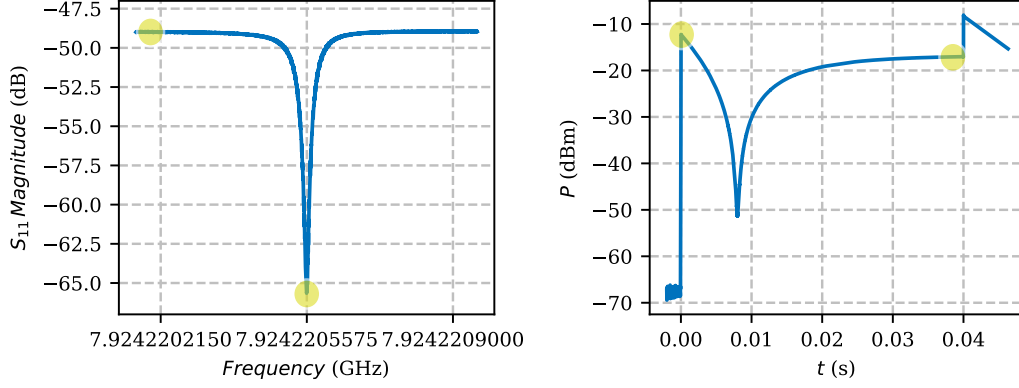
Figure 5.9: Comparison of the time domain power measurement (right) and frequency domain scattering parameter measurement (left). Shown in yellow is $|S_{11}|$ on and off resonance and its related reflected power levels of the steady state and the immediate response of the resonator after switching on the drive.

by further investigating equation 5.5. The first peak of the reflected power during the ring up is proportional to P_f. A constant plateau of the reflected power P_r is reached with long enough ($\gg \tau$) drive pulses.

$$P_\mathrm{r} = P_\mathrm{f}\left(1 - \frac{2\beta}{1+\beta}\right)^2 = P_\mathrm{f}\left(\frac{1-\beta}{1+\beta}\right)^2 \tag{5.15}$$

The outcome is identical with equation 5.14. The expression for the coupling parameter $\beta > 1$ follows

$$\beta = \frac{1 + \sqrt{P_\mathrm{r}/P_\mathrm{f}}}{1 - \sqrt{P_\mathrm{r}/P_\mathrm{f}}} \tag{5.16}$$

The detection of the power levels P_r and P_f leads to a coupling parameter for every drive power. With the relations between the known parameter Q_l and β

$$Q_\mathrm{int} = Q_\mathrm{l}(\beta + 1) \quad \text{and} \quad Q_\mathrm{c} = \frac{Q_\mathrm{l}(\beta + 1)}{\beta} \tag{5.17}$$

the coupling and the internal quality factors can be calculated for each reflected power trace. The results are shown in figure 5.10. The constant behaviour of $Q_\mathrm{c} \sim 2.5 \cdot 10^8$ as well as the rising internal quality factor up to $Q_\mathrm{int} \geq 1.1 \cdot 10^9$ with higher input power levels can be confirmed. At low input power levels the internal quality factor remains at a constant plateau of $Q_\mathrm{int} \sim 0.5 \cdot 10^9$, where the enhanced measurement noise increases the uncertainty of the quality factors obtained in the time domain.
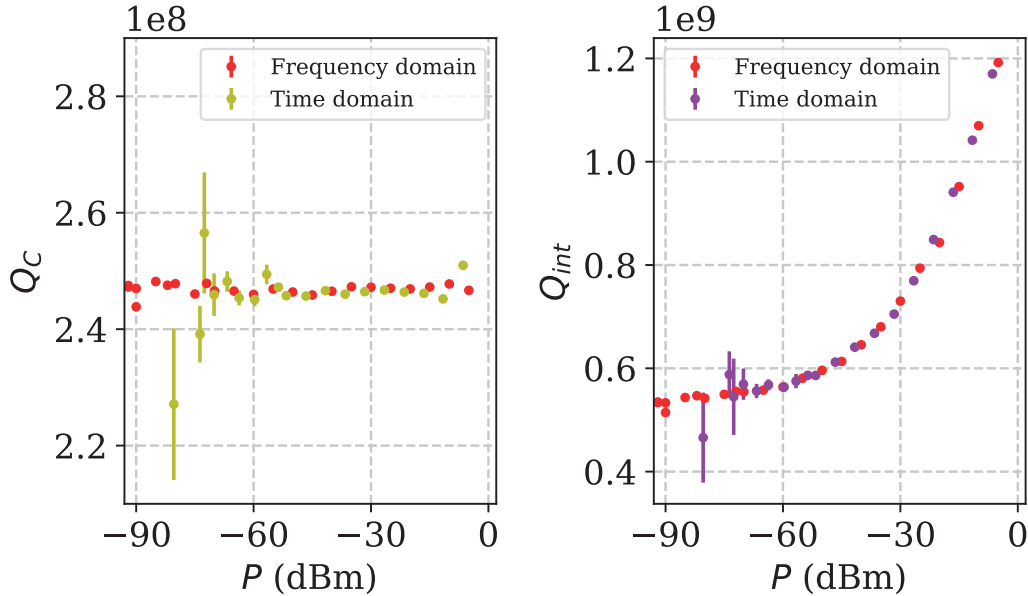
Figure 5.10: Coupling and internal quality factors at different drive power levels obtained with Q_1 values from the power decay combined with the corresponding coupling strength β. The latter is extracted by the ratio of the reflected power response at the steady state and right after switching on the power drive. Furthermore the circlefit data of VNA measurements (red) is shown.

5.7 Laplace transform intermezzo

The Laplace transform is a powerful tool to analyse linear dynamical systems. This section gives a short introduction to the Laplace transform and its applications. It is based on [39], appendix A. Furthermore the transient and decay behaviour of a resonator in the reflection are investigated using the Laplace and the inverse Laplace transform formalism.

The Laplace transform is an integral transform closely related to the Fourier transform. It is restricted to functions of time $f(t)$, which vanish for times $t < 0$. For such functions, the Laplace transform $\mathcal{L}\{f(t)\}$ is defined as

$$\mathcal{L}\{f(t)\} = F(s) = \int_0^\infty f(t)e^{-st}\,dt \tag{5.18}$$

with the complex number frequency parameter $s = \sigma + j\omega$. The inverse Laplace transform back in to the time domain is defined as

$$\mathcal{L}^{-1}\{F(s)\} = f(t) = \frac{1}{2\pi j}\int_{\sigma_0-j\infty}^{\sigma_0+j\infty} F(s)e^{st}\,ds \tag{5.19}$$

56

The convolution and derivative properties of the Laplace transform are given by

$$\mathcal{L}\{f_1(t) * f_2(t)\} = F_1(s) \cdot F_2(s) \tag{5.20}$$

$$\mathcal{L}\{\frac{df(t)}{dt}\} = s \cdot F(s) - f(0^+) \tag{5.21}$$

Equation 5.21 reveals the utility of the Laplace formalism. A differential equation in the time domain gets Laplace-transformed to an algebraic equation. After solving the algeabric equation, the inverse Laplace transform leads to the solution in the time domain. Another handy property is displayed in equation 5.20, which shows that a convolution in the time domain translates as a multiplication in the (complex) frequency domain.

In the case of a resonator in reflection configuration, the scattering parameter S_{11} resembles its transfer function

$$h(\omega) = \frac{V_{\text{out}}(\omega)}{V_{\text{in}}(\omega)} = \frac{2Q_{\text{l}}/Q_{\text{c}}}{1 + 2jQ_{\text{l}}\frac{\omega - \omega_0}{\omega_0}} - 1 \tag{5.22}$$

For the stored energy in the cavity to be zero at $t = 0$, the transfer function can be rewritten with the complex parameter $j\omega \rightarrow s$ to

$$h(s) = \frac{2Q_{\text{l}}/Q_{\text{c}}}{1 + \frac{2Q_{\text{l}}s}{\omega_0} - 2jQ_{\text{l}}} - 1 = \frac{2/(1 + \beta^{-1})}{1 - 2jQ_{\text{l}} + 2Q_{\text{l}}s/\omega_0} - 1 \tag{5.23}$$

This is a preparatory step to make use of equation 5.20, where a convolution gets transformed into a multiplication. The resonant signal pulse in the time domain starting at $t = a$ and ending at $t = e$ is modelled with

$$V_{in}(t) = V_{\text{f}} \cdot \Theta(t - a) \cdot \Theta(-t + e)\Big(\cos\left(\omega_0 t\right) + j\sin\left(\omega_0 t\right)\Big) \tag{5.24}$$

assuming $e \geq a \geq 0$. $\Theta(t)$ depicts the Heaviside step function, V_{f} the voltage amplitude. The next step is to Laplace transform $V_{in}(t)$ and multiply it with the transfer function $h(s)$. The following inverse Laplace transform of the latter product leads to an expression for the output signal $V_{out}(t)$ in the time domain.

$$V_{out}(t) = \mathcal{L}^{-1}\{\mathcal{L}\{V_{in}(t)\} \cdot h(s)\} \tag{5.25}$$

The actual solving of the Laplace integrals is done with the software Mathematica [40]. The full code can be found in listings 2, appendix C. The result for the reflected power signal of the cavity response to a resonant drive pulse starting at

$t = a$ and ending at $t = e$ is

$$P_r(t) = |V_{out}(t)|^2 = \begin{cases} P_{\mathrm{f}} \dfrac{e^{-\frac{\omega_\circ t}{Q_{\mathrm{l}}}} \left((\beta - 1)e^{\frac{\omega_\circ t}{2Q_{\mathrm{l}}}} - 2\beta e^{\frac{\omega_\circ a}{2Q_{\mathrm{l}}}}\right)^2}{(\beta + 1)^2} & \text{if } a \leqslant t < e \\[4mm] P_{\mathrm{f}} \dfrac{4\beta^2 e^{-\frac{\omega_\circ t}{Q_{\mathrm{l}}}} \left(e^{\frac{\omega_\circ a}{2Q_{\mathrm{l}}}} - e^{\frac{\omega_\circ e}{2Q_{\mathrm{l}}}}\right)^2}{(\beta + 1)^2} & \text{if } t \geqslant e \end{cases} \tag{5.26}$$

where $P_{\mathrm{f}} = |V_f|^2$ depicts the input signal power. The reflected power's steady state P_{r}^{ss} is obtained by evaluating equation 5.26 considering only the ring up in the limit of $t \to \infty$ with the drive switched on at $a = 0$

$$P_{\mathrm{r}}^{ss} = P_{\mathrm{f}} \frac{(\beta - 1)^2}{(\beta + 1)^2} \tag{5.27}$$

The immediate peak at the switch on is derived from the ring up term in the limit of $t \to a$

$$P_{\mathrm{r}}^* = P_{\mathrm{f}} \tag{5.28}$$

Further investigating the power decay term in 5.26 leads to the reflected power peak P_{r}^d at the start of the decay. Arguing that the cavity reached the steady state before the switch off, the relation between the switch on and off times $e \gg a$ justifies the simplification

$$\left(e^{\frac{\omega_\circ a}{2Q_{\mathrm{l}}}} - e^{\frac{\omega_\circ e}{2Q_{\mathrm{l}}}}\right)^2 \approx e^{\frac{\omega_\circ e}{Q_{\mathrm{l}}}} \tag{5.29}$$

With this consideration, the ring down term of equation 5.26 in the limit of $t \to e$ becomes

$$P_{\mathrm{r}}^d = P_{\mathrm{f}} \frac{4\beta^2}{(\beta + 1)^2} \tag{5.30}$$

The findings of the cavity's transient and decay behaviour, responding to a resonant drive pulse, using the Laplace transform formalism are consistent with the results of H. Padamsee et al. [30]. By introducing a small detuning δ to the input signal and considering only the transient behaviour with the cavity drive switched on at $t = 0$, equation 5.24 is modified to

$$V_{in}(t) = V_{\mathrm{f}} \, \Theta(t) \Big(\cos\left(2\pi(f_0 + \delta)\, t\right) + j \sin\left(2\pi(f_0 + \delta)\, t\right) \Big) \tag{5.31}$$

The solution of the ring up for the the reflected power signal including a detuned

cavity drive is then given by

$$P_r(t) = \frac{P_f}{(\beta + 1)^4 \left(4\delta^2 l^2 + f_0^2\right)} \Big[4\beta^2 (\beta + 1)^2 f_0^2 e^{-\frac{2\pi f_0 t}{Q_l}}$$
$$+ \left(\beta^2 - 1\right)^2 f_0^2 + 4(\beta + 1)^4 \delta^2 Q_l^2 -$$
$$4\beta(\beta + 1)^2 f_0 e^{-\frac{\pi f_0 t}{Q_l}} \left(2(\beta + 1)\delta Q_l \sin(2\pi\delta t) + (\beta - 1) f_0 \cos(2\pi\delta t)\right)\Big] \quad (5.32)$$

The Mathematica script leading to this expression is presented in listings 3, appendix C.

5.8   The rewards of understanding the ring up

In this section the reflected power behaviour in the time domain after switching on the drive power is examined with the analytical fit functions derived in the previous section. Each ring up trace, corresponding to a different input drive power, is fitted with equation 5.5, assuming a resonant cavity drive. Two ring up traces, one in the high and one in the low input power regime, are displayed in figure 5.11. The effect of disregarding a detuned cavity drive can be detected in the logarithmic plots, as the fit function minimum aims for the zero power line. After that, each trace is approximated with equation 5.6, considering a detuned cavity drive. The fitted reflected power ring up traces, for two different cavity drive output levels are shown in figure 5.14. The logarithmic power scale reveals an improvement of the fitted curves, as the fit functions take into account the rf drive detuning.

The results of both fit options are shown in figure 5.12 and 5.13. The extracted quality factors show similar behaviour for both, the resonant and the detuned ring up fit options. Compared to the circlefit data measured in the frequency domain, Q_l, Q_{int} and even Q_c get overestimated for high input power levels. This is a rather surprising result, as Q_c should stay constant, because the coupling pin is unaltered during the ring up. The internal quality factor Q_{int} is expected to vary during the filling of the cavity, as the saturation of two-level-systems proceeds with an increasing inner cavity energy. On the contrary, the ring up fit functions assume a constant Q_{int} during the transient response. In that sense, the deviation of the fit extracted quality factors is explicable. The rise of the Q_c levels at high input power can be explained by the correlation of the fit parameters. Lowering Q_{int} has the same effect on the ring up curve as a rise in the coupling quality factor Q_c. The overestimation of Q_c partially compensates the Q_{int} power dependence. At low power levels, where the power dependence of Q_{int} decreases,

both fit options match with the circlefit data. A slight superior behaviour of the ring up fit including drive detuning can be detected .

The quality of a fit can be demonstrated by looking at its residuals

$$r_i = Y_i^{data} - Y_i^{fit} \tag{5.33}$$

where the distance between the data points Y_i^{data} and the fit function Y_i^{fit} is calculated. At high power levels, the residuals, plotted over time show a pattern in both fit options, indicating a variation of Q_{int} during the ring up. At low power, the pattern vanishes as the internal quality factor stays constant. The variation of noise levels in the low input power residuals plot comes from a modified measurement sensitivity of the spectrum analyzer at different input power levels.

For the execution of the resonant ring up fit, the common least square method is used, where the sum of the squared residuals is minimized. In the case of the detuned ring up fit, the least square fitting method tends to disregard the detuning. Due to this reason, a weighted least squares fit is implemented. To make the fit take into account the nonzero minimum of the ring up curve, which is responsible for the extent of the detuning, the weighted sum of squares

$$\sum_i \left(\frac{Y_i^{data} - Y_i^{fit}}{Y_i^{data}} \right)^2 \tag{5.34}$$

is minimized as part of the fit at high power levels. At low power levels instead of the weighting, a lower boundary for the fit parameter δ is introduced. It is set to $\delta_{min} = 0.1\,\mathrm{Hz}$, which corresponds to the lowest fitted value for δ.
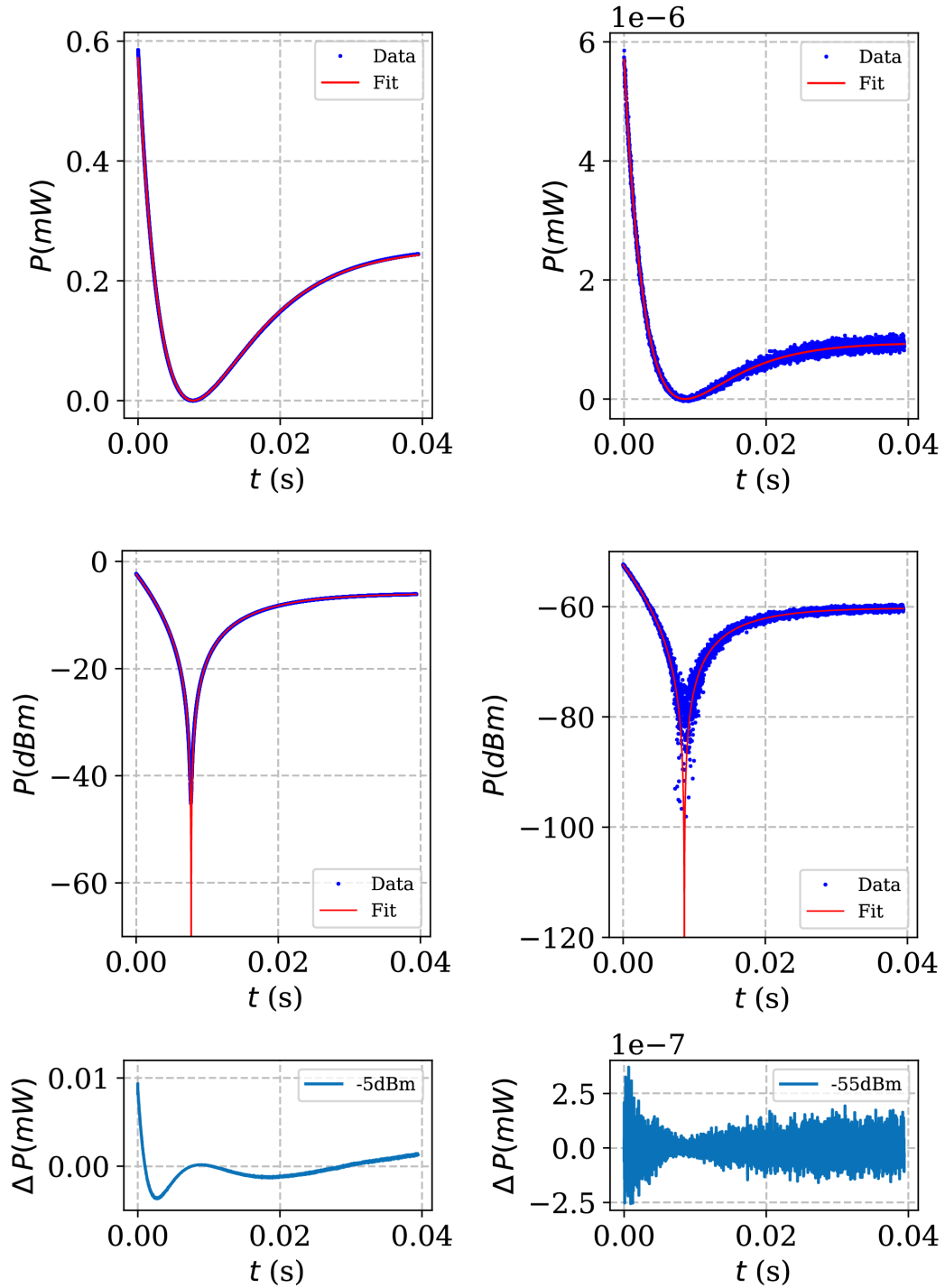
Figure 5.11: The time domain cavity reflected power ring up traces in the linear (upper panel) and logarithmic scale (middle panel) for two different drive output power levels of $-5\,\mathrm{dBm}$ (left) and $-55\,\mathrm{dBm}$ (right). Furthermore the fit functions (red lines), considering a resonant drive pulse are shown. In the lower panel, a plot of the corresponding fit residuals is displayed.
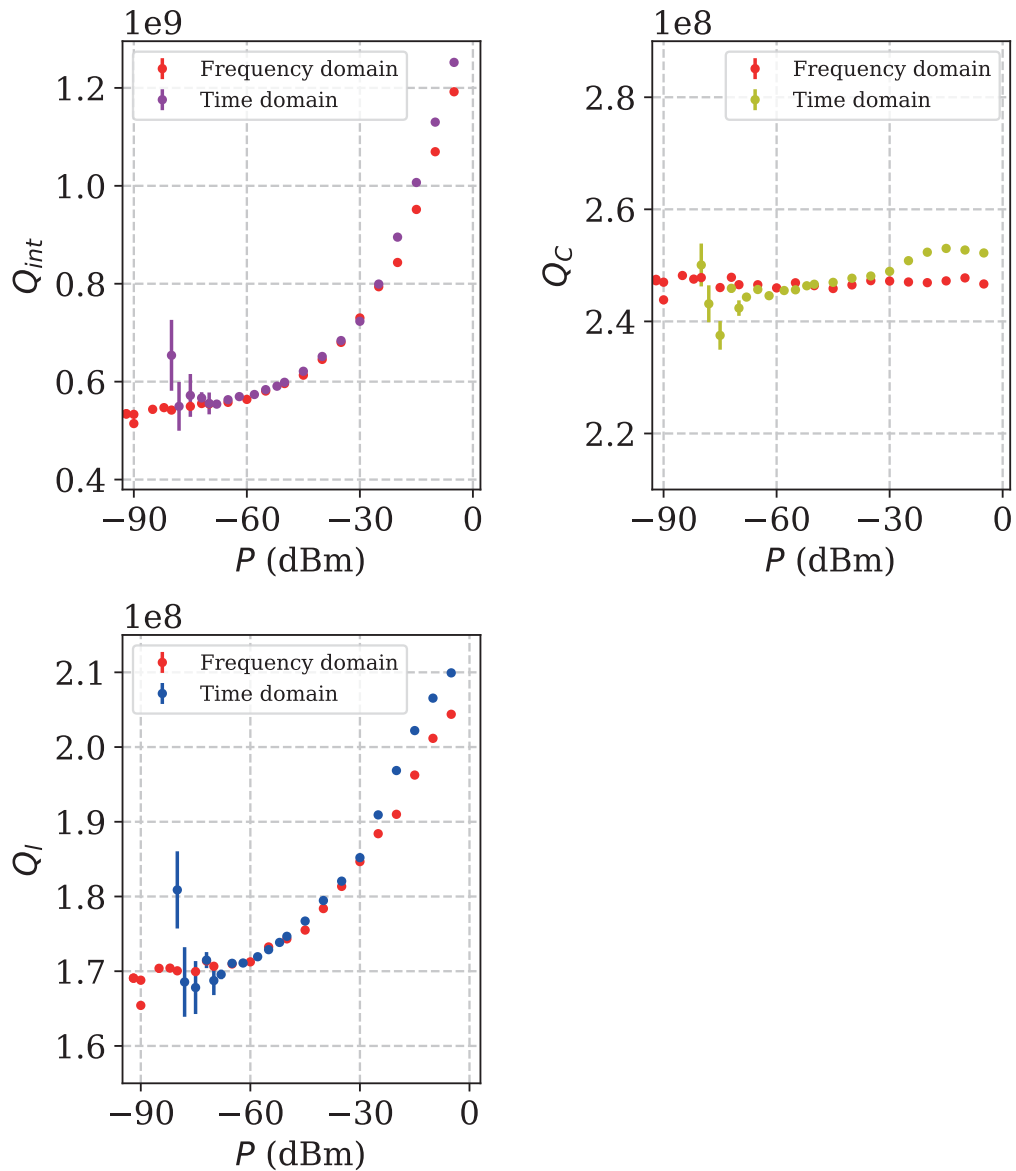
Figure 5.12: Extracted quality factors as a function of the cavity drive output power from analysing the transient behaviour of the reflected power signal with an analytic fit function that assumes a resonant drive pulse. Further shown are quality factors from frequency domain measurements.
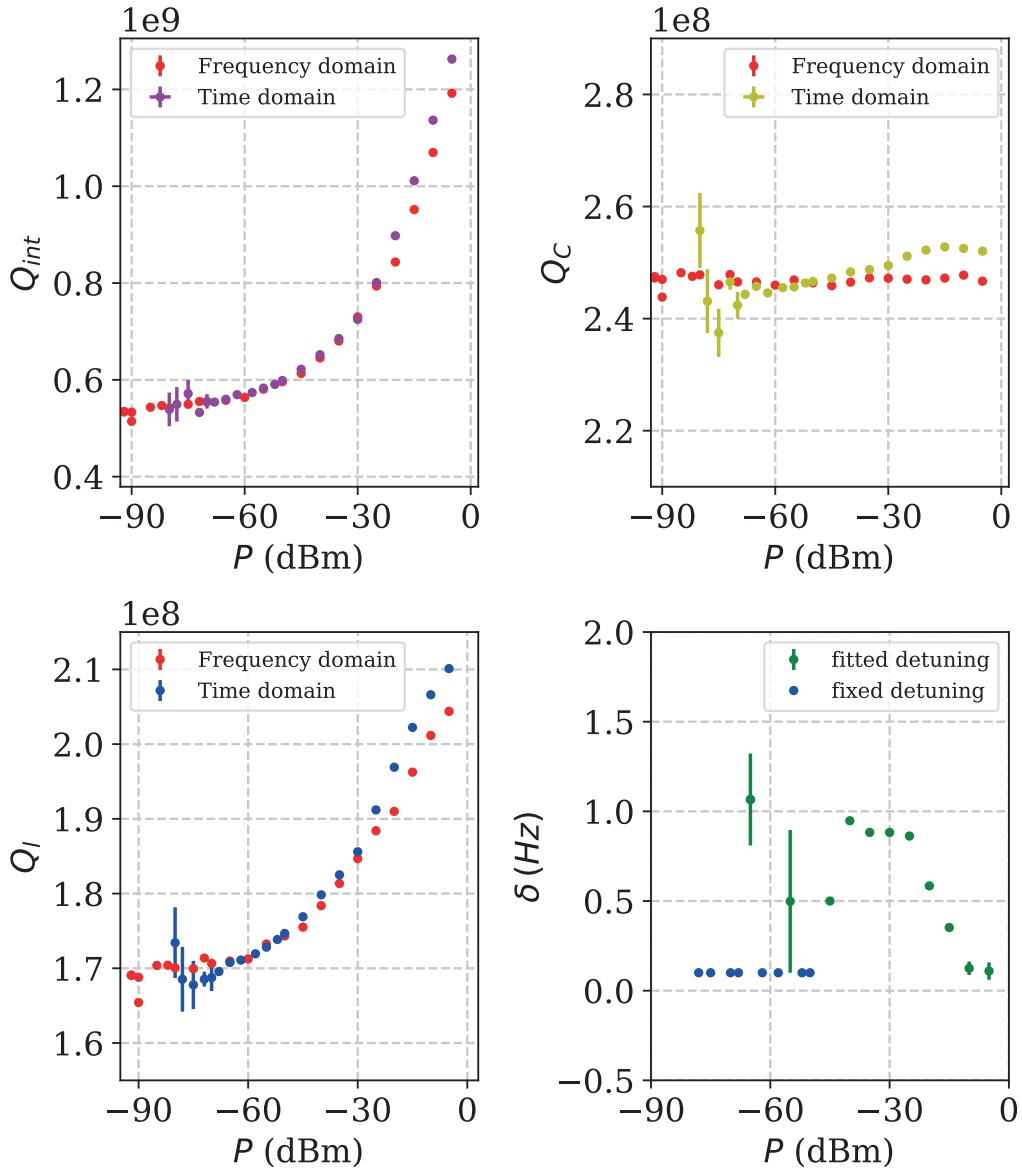
Figure 5.13: Quality factor results as a function of the cavity drive output power of the transient reflected power response considering an analytical fit function that permits a detuned input signal compared to frequency domain measurements. The extracted quality factors are similar to the prior obtained results from the resonant ring up fit. Furthermore, the fit results for the cavity input signal detuning δ (lower right) are displayed. If the fit at a certain input power level converged but δ remained at the lower boundary level, the detuning is marked blue.
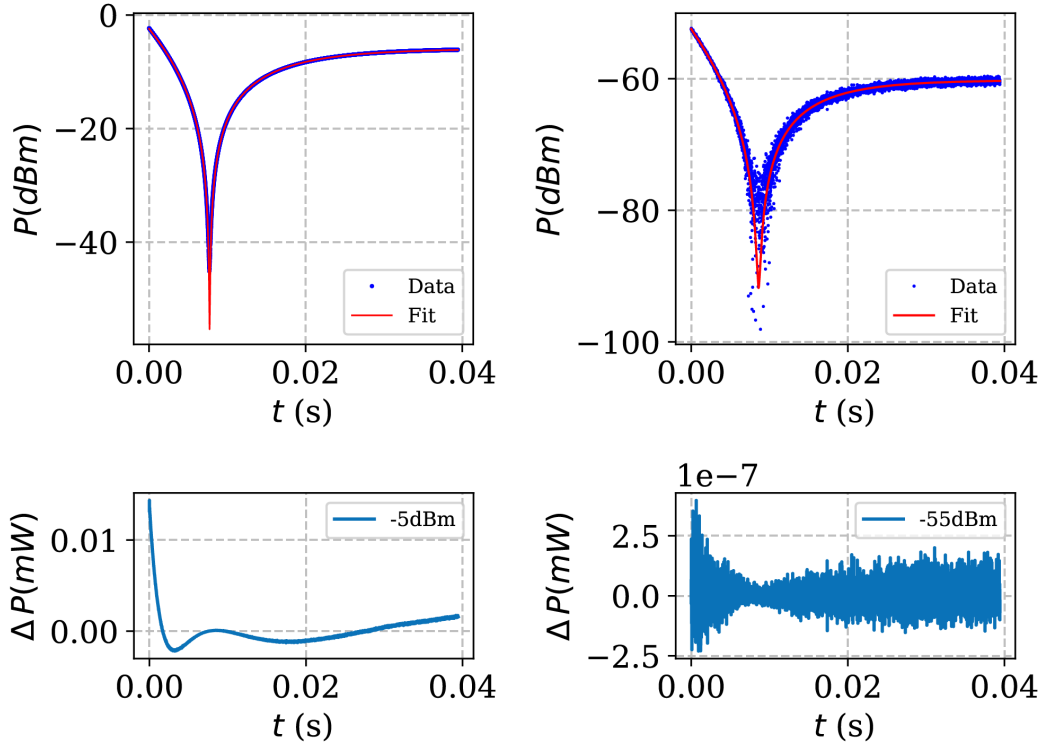
Figure 5.14: Cavity reflected power ring up traces in the logarithmic scale for two different drive output power levels of $-5\,\mathrm{dBm}$ (left) and $-55\,\mathrm{dBm}$ (right). Additionally, the fit functions, including a rf drive detuning, are plotted (red lines). In the lower panel, a plot of the corresponding fit residuals is shown.

5.9 Time domain analysis of the aged niobium cavity

The time domain measurement series of the niobium coaxial cavity is repeated after months of ageing not preserved in a vacuum desiccator. The purpose of this measurement series is to confirm the issue of a growing dielectric layer on the inner cavity walls, leading to bigger internal losses and a decreased Q_{int}. Moreover, the experiment repetition is made with the intention of approving the analytical ring up fit formula 5.6 and the numerical fit routine from section 5.5, in the case of a less power dependent quality factor.

The cavity reflected power trace responding to a (almost) resonant drive pulse is shown in figure 5.16. The shape of the curve with the more equalized peak heights and the lowered steady state value already reveals the reduced coupling strength β. See figure 5.1 for the impact of a changed coupling strength on the reflected power curve and, for comparison, a reflected power trace of the previous measurement series in figure 5.4.

After subtracting the noise floor, as shown in section 5.4, the numerical fit

routine is applied. The Q_l data, obtained from the decay's slope in each power slice, is depicted in figure 5.15. In contrast to previous results (see figure 5.7), the high input power Q_l traces of the aged niobium cavity agree well with the frequency domain reference measurements. It seems that a resonator, with a weak power dependent loaded quality factor, can be analyzed well with the numerical fit method. Given the right circumstances, one can resolve the power dependence of Q_l over the whole measurement range within a single pulsed reflected power measurement. In this particular case, a 50 dB attenuator prevents the continuation of the Q_l traces to lower power values, since the decay traces vanish in the spectrum analyzer's inherent noise.
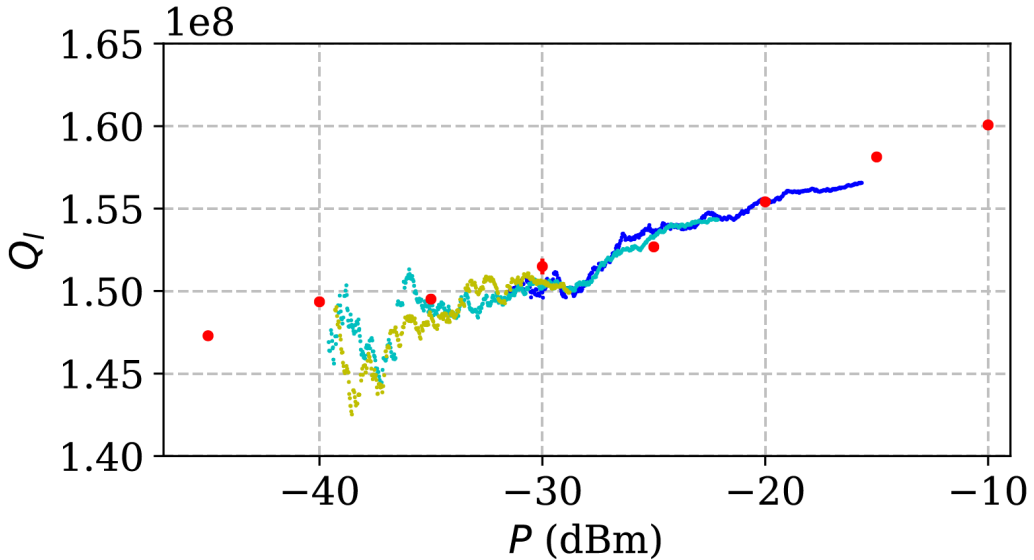
Figure 5.15: Loaded quality factor Q_l traces for three different input pulse power levels extracted from a numerical power decay fit compared to circlefit reference data (red dots) as a function of the cavity input drive power measured in the frequency domain. Each of the blue, cyan or yellow coloured dots represents a numerical fitted Q_l value, depending on the power level leaking out the cavity.

The actual reflected power trace of the cavity's transient behaviour for an input power of -10 dBm and the corresponding fit function, considering a detuned cavity drive, is shown in figure 5.16. The results of the fit process are further shown in figure 5.17. The fits agree well with the measured data. Due to the less pronounced power dependency of Q_{int} and Q_l respectively, the reflected power traces were only taken at high input power. The extracted quality factors match with the circlefit data. The ring up fit quality benefits from the rather constant Q_{int}, as displayed in the high power residuals plot that shows no distinct pattern. The bigger errorbars compared to previous results at similar power levels are due

to an additional attenuator in front of the spectrum analyzer input, which gives rise to a lower signal to noise ratio and bigger fit uncertainty. The detuning stays constant slightly above 1 Hz, which is a convincing inaccuracy as a consequence of measurement uncertainty. For the data analysis of this measurement series neither a lower boundary for δ, nor a weighted fit model is needed.
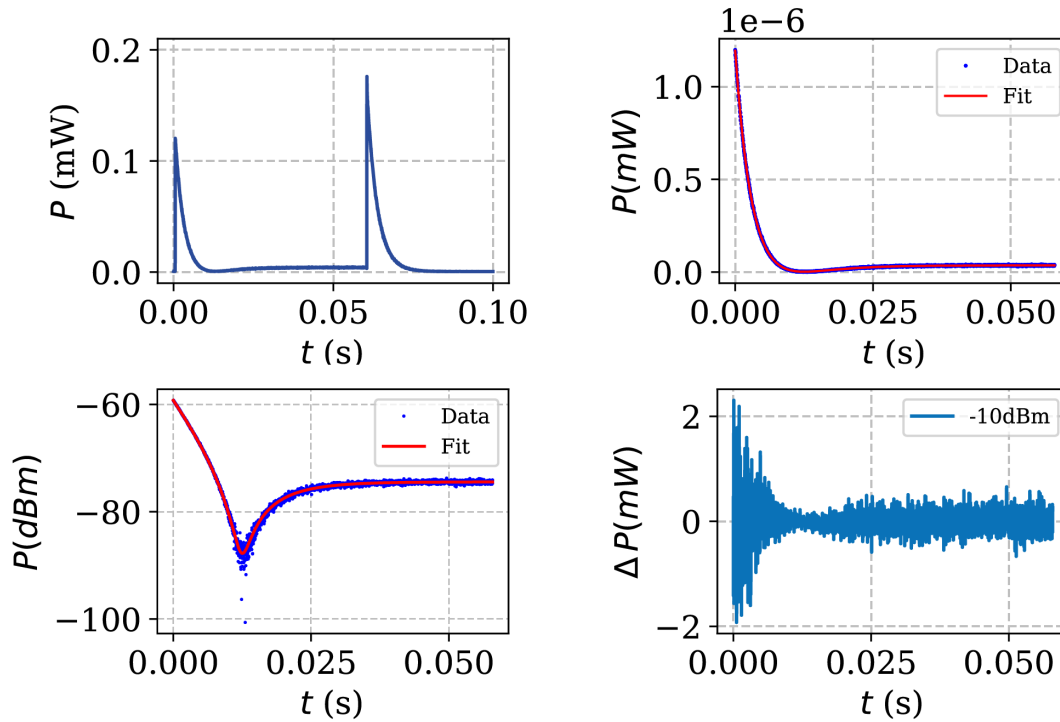
Figure 5.16: Upper left: Aged niobium cavity reflected power trace in the time domain responding to a $-10\,\text{dBm}$ resonant drive pulse. **Upper right:** Ring up segment of the aged niobium cavity reflected power trace in the linear power scale at a drive output of $-10\,\text{dBm}$. Additionally, the fit function, including a rf drive detuning is plotted (red line). **Lower left:** Same $-10\,\text{dBm}$ rf drive output reflected power trace and the ring up fit, regarding a detuned cavity drive, in the logarithmic scale. **Lower right:** Plot of the corresponding fit residuals.
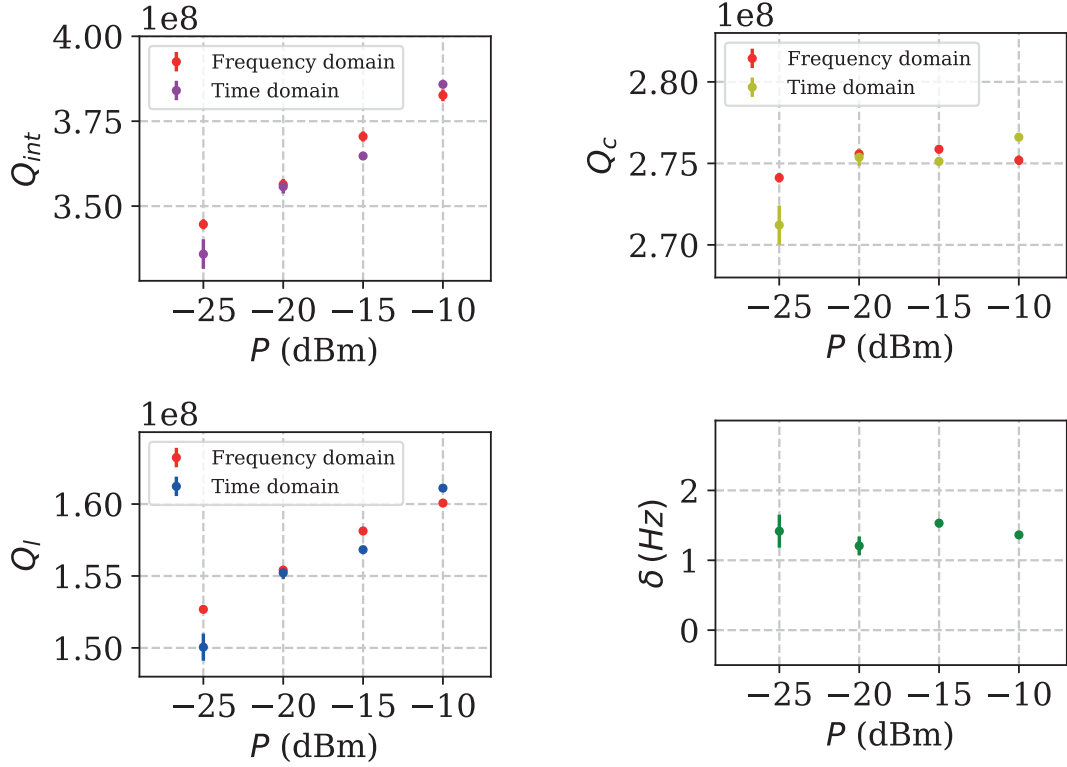
Figure 5.17: Ring up analysis results of the reflected power trace of the aged niobium coaxial cavity. The power dependence of the quality factors, extracted from an analytical ring up fit function that includes a detuned cavity drive, compared to frequency domain measurements of the aged niobium coax cavity are displayed. Additionally, the ring up fit results for the cavity input signal detuning δ (lower right) are shown.

5.10   Summary

Probing a resonator in the time domain turns out to be an advantageous measurement technique to confirm the high internal quality factor of the niobium coaxial quarterwave resonator ranging from $Q_{\mathrm{int}} \sim 0.5 \cdot 10^9$ at low input power level and $Q_{\mathrm{int}} \geq 1.1 \cdot 10^9$ in the high input power limit. Examining the distinct shape of the cavity response to a resonant drive pulse reveals the coupling regime and, if the cavity is under-coupled, a potential drive detuning. The decay of the cavity reflected power, after switching off the drive, provides the loaded quality factor Q_{l}. Further knowledge of the reflected power levels of the steady state and the immediate peak after switching on the drive leads to the coupling and internal quality factors Q_{c} and Q_{int}. Making use of the Laplace transform, an analytic expression for the cavity reflected power is derived. Furthermore an expression for the transient cavity behaviour including a detuned drive is obtained.

As the power decay characteristic of the niobium coax cavity, after switching off the drive, is not purely exponential, a numerical fit is implemented to obtain Q_{l}. The result is a trace of decreasing Q_{l} values, depending on the power leaking out the cavity. The Q_{l} traces, corresponding to low input power pulses, and the first Q_{l} values of the high input power pulses are in agreement with the circlefit data measured in the frequency domain. Following the traces, which involve a significant change of Q_{int} during the decay, a deviation from the reference data emerges. This suggests further analysis aiming for an analytic expression of the Q_{int} power dependence. By fitting the analytic ring up expressions, regarding and disregarding a detuned cavity drive, to the transient reflected power data, the quality factors get obtained from the fit parameters. The results of the cavity ring up fits are in good agreement with the circlefit data measured in the frequency domain. At high input power levels a slight divergence from the reference data is detected. This can be explained by the fit assuming a constant Q_{int} over the ring up process. A small detuning $\delta < 1.5\mathrm{Hz}$ of the cavity drive is detected. Repeating the measurements of the same, but aged cavity yields in lower results for the internal quality factor of $Q_{\mathrm{int}} \sim 0.375 \cdot 10^9$ at high input power levels, due to increased dielectric losses at the cavity walls. A less pronounced power dependency of the loaded and internal Q factor is observed, from which both, the numerical decay and the ring up fit method benefit.

6   Conclusion

The copper coaxial $\lambda/4$ resonators yielded the lowest quality factor results, since the resonator design possesses a rather high magnetic participation ratio for normal conducting metals. Both surface treatments etching and annealing proofed to be advantageous. As a result, internal quality factors in the range of 10^4 were achieved. Reducing material defects during the fabrication process and refining the etching process, for example by monitoring the oxidation redox potential of $CuCl_2$ [23], would probably cause less surface resistance and therefore less conductive losses.

The aluminum cavities showed internal quality factors up to $\sim 10^7$. Changing the cavity machining technique from drilling to sinker electrical discharge machining and optimizing the cavity design parameters revealed a beneficial effect. Still, fabrication and surface treatment fine tuning should lead to enhanced internal quality factors of about $\sim 10^8$, as reported in [7].

The niobium Q-improvement, involving the buffered chemical polishing method turned out well, as the achieved internal quality factor is in the range of 10^9. Further examination of various annealing or baking methods could lead to even higher quality factors. Especially the $340°\,C$ vacuum heat treatment, as reported in [36], seems to be a promising approach.

The investigations on the cavity reflected power traces in the time domain, responding to a resonant drive pulse, yielded a robust method to extract resonator characterising parameters. In particular, if the trend of increasing quality factors proceeds, VNA resonator measurements in the frequency domain could get challenging with decreasing resonance line widths. The loaded quality factor of the resonator can be derived via numerical analysis of the measured power, which is leaking out of an excited cavity. By further studying the enhanced Q_l values, obtained from the late stages of the decay, new insights about long-lived two-level-systems or quasi particle recombinations could be derived.

Appendices

A   Experimental setup picture
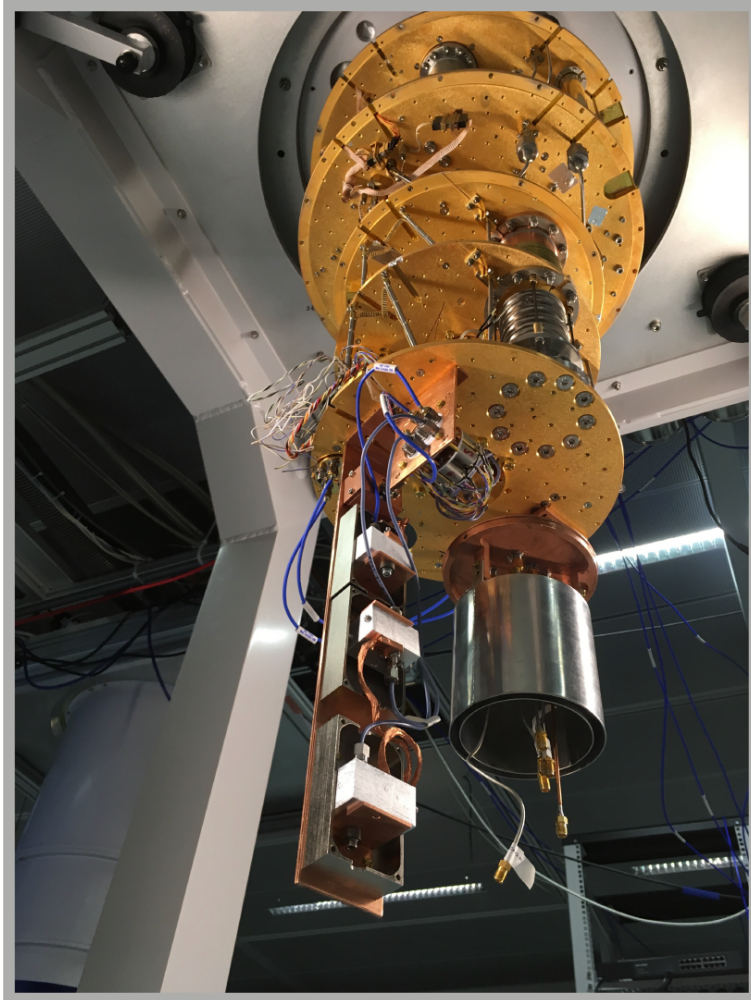
Figure A.1: Bottom view of the experimental setup inside the dilution refrigerator. One copper and three aluminum coaxial quarterwave cavities are mounted on the cryostat's baseplate in reflection configuration with the aid of a microwave switch. The aluminum resonators are situated inside (half opened) magnetic shields. Copper braids assist the resonator's thermalization.

B   Python code of the numerical fit routine

```python
import numpy as np
for s in np.arange(len(dmb2log)):
    end=len(np.array(dmb2log[s].y))-np.nanargmax(dmb2log[s].y)
    -100
    Ql[s]=[]
    Ql_err[s]=[]
    P[s]=[]
    P_raw_err=[]
    P_raw[s]=[]
    Power_a=[-5, -25, -40, -55, -70, -75, -80]
    Power_b=[-10, -15, -20, -30, -35, -45, -50, -52, -58, -62,
    -65, -68, -72, -78]
    deltaP=np.nanmax(dmb2log[s].y)-Power_b[s]

    for i in np.arange(0, end, 10):
            a=np.nanargmax(dmb2log[s].y)
            a= a+10+i
            y=dmb2log[s].y[a:a+400]
            x=dmb2log[s].x[a:a+400]
            perr=np.std(y)
            P[s].append(np.nanmean(y)-deltaP)
            P_raw[s].append(np.nanmean(y))
            idx = np.isfinite(dmb2log[s].x)
            & np.isfinite(dmb2log[s].y)
            fit,cov=np.polyfit(x[idx[a:a+400]],
            y[idx[a:a+400]],1, cov=True)
            stderr=np.sqrt(np.diag(cov))
            Q=7.924224544e9/(1/(2*np.pi*(
            -(fit[0]/10*np.log(10))**-1)))
            Q_err=7.924224544e9*2*np.pi*10/
            (fit[0]**2*np.log(10))*stderr[0]
            Ql_err[s].append(Q_err)
            Ql[s].append(Q)

    Q_all_b.append(Ql[s])
    P_all_b.append(P[s])
    P_all_b_raw.append(P_raw[s])
    Q_all_b_err.append(Ql_err[s])
```

Listing 1: Python code of the numerical fit routine.

C   Laplace Transform Mathematica Code

```
1  (FullSimplify[
2    InverseLaplaceTransform[(LaplaceTransform[(HeavisideTheta[t - (
     e)]*
3         HeavisideTheta[-t + (f)])*(Cos[(r)*2 Pi*t] +
4         I*Sin[(r)*2 Pi*t]), t, s,
5       Assumptions ->
6        e < f])*(((2/(1 + 1/b))/((1 + 2*l/(r*2 Pi)*s - 2*I*(l))) -
7         1)), s, t]])
8  (*Laplacetransform a resonant Input pulse starting at time e and
     \
9  ending at f*)
10 (*Inverse Laplacetransform previous result times \
11 transfrefunction, which is in this case equivalent to the
     reflection \
12 scattering parameter S_11*)
13
14 ((Abs[1/(1 + b) E^(((-1 + 2 I l) \[Pi] r t)/l) ] //
15     ComplexExpand) ((-1 + b) E^((\[Pi] r t)/
16       l) (HeavisideTheta[-e + t] - HeavisideTheta[-f + t] +
17         HeavisideTheta[-e, f] - HeavisideTheta[-e, -e + t] +
18         HeavisideTheta[-e, -f + t] - HeavisideTheta[-e, f, -f + t
     ]) +
19     2 b (-HeavisideTheta[-e, f] +
20       E^((e \[Pi] r)/
21         l) (-HeavisideTheta[-e + t] + HeavisideTheta[-e, -e + t
     ]) +
22       E^((f \[Pi] r)/
23         l) (HeavisideTheta[-f + t] - HeavisideTheta[-e, -f + t]
     +
24          HeavisideTheta[-e, f, -f + t])))))^2
25
26
27 (* (Abs[]// complex expand) makes the expression for the result
     signal
28 real. Squaring it brings power equivalent*)
29
30 (*simplify expression*)
31
32 FullSimplify[
33  1/(1 + b)^2 E^(-((2 \[Pi] r t)/
34    l)) ((-1 + b) E^((\[Pi] r t)/
35      l) (HeavisideTheta[-e + t] - HeavisideTheta[-f + t]) +
36    2 b (+E^(((e \[Pi] r)/l)) (-HeavisideTheta[-e + t]) +
```

72

```mathematica
37      E^((f \[Pi] r)/l) (HeavisideTheta[-f + t])))^2, {e >= 0,
38    f >= e, t >= e}]
39
40
41  FullSimplify[
42   1/(1 + b)^2 E^(-((2 \[Pi] r t)/
43     l)) ((-1 + b) E^(((\[Pi] r t)/
44       l) (HeavisideTheta[-e + t] - HeavisideTheta[-f + t]) +
45     2 b (+E^(((e \[Pi] r)/l)) (-HeavisideTheta[-e + t]) +
46       E^((f \[Pi] r)/l) (HeavisideTheta[-f + t])))^2, {e >= 0,
47    f >= e, e < t < f}](*ringup function for e<t<f*)
48
49  FullSimplify[
50   1/(1 + b)^2 E^(-((2 \[Pi] r t)/
51     l)) ((-1 + b) E^(((\[Pi] r t)/
52       l) (HeavisideTheta[-e + t] - HeavisideTheta[-f + t]) +
53     2 b (+E^(((e \[Pi] r)/l)) (-HeavisideTheta[-e + t]) +
54       E^((f \[Pi] r)/l) (HeavisideTheta[-f + t])))^2, {e >= 0,
55    f >= e, t > f}](*ringdown function for t>f*)
56
57  TrueQ[Simplify[
58    Expand[(-2 b E^((e \[Pi] r)/l) + (-1 + b) E^(((\[Pi] r t)/l))
59     ^2],
60    e == 0] ==
61   Simplify[Expand[(E^(((\[Pi] r t)/l) -
62       b (-2 + E^(((\[Pi] r t)/
63         l)))^2]]](*check if reflected power formula from H.
64    Padamsee is equal*)
65
66  Manipulate[
67   Plot[{1/(1 + b)^2 E^(-((2 \[Pi] r t)/
68     l)) (-2 b E^((e \[Pi] r)/l)
69       HeavisideTheta[-e + t] + (-1 + b) E^(((\[Pi] r t)/
70       l) (HeavisideTheta[-e + t] - HeavisideTheta[-f + t]) +
71     2 b E^((f \[Pi] r)/l) HeavisideTheta[-f + t])^2}, {t, -5,
72     10},
73    PlotRange -> {0, Full}], {{b, 3}, 0.1, 10}, {{r, 500}, 100,
74    1000}, {{l, 300}, 100, 1000}, {{e, 1}, -5, 10}, {{f, 4}, 0,
75    10}](*plot result*)
76
77  Limit[Simplify[(
78    E^(-((2 \[Pi] r t)/
79     l)) (-2 b E^((e \[Pi] r)/l) + (-1 + b) E^(((\[Pi] r t)/l))^2)
80     /(1 +
81     b)^2, {l == C, r == C}],
```

73

```
78  t -> Infinity](*check steady state limit of ringup formula*)

79

80 Limit[(Simplify[(
81     4 b^2 E^(-((2 \[Pi] r t)/l)) (-E^(((f \[Pi] r)/l)))^2)/(1 +
82       b)^2, {l == C, r == C}]), f -> t]

83

84 (*check inital power value P_0 of exponential decay of ringdown
       formula*)
```

Listing 2: Mathematica Script for the analytical expression of the resonator response to a resonant drive pulse.

```
1 A = LaplaceTransform[
2   HeavisideTheta[
3     t]*(Cos[(r + \[Delta])*2 Pi*t] + I*Sin[(r + \[Delta])*2 Pi*t
    ]), t,
4     s]
5 S11s = ReplaceAll[2 l/c/(1 + 2*l/(r*2*Pi)*s - 2*I*l) - 1,
6   l -> 1/(1/i + 1/c)]
7 R1 = FullSimplify[InverseLaplaceTransform[A*S11s, s, t]]
8 R2[t_, i_, r_, c_, \[Delta]_] =
9  FullSimplify[(Abs[R1] // ComplexExpand)^2]
10 R3 = R[t_, i_, r_, c_, \[Delta]_] =
11   1/((c + i)^2 r^2 + 4 c^2 i^2 \[Delta]^2)
12     Simplify[
13     Expand[(2 c i \[Delta] Cos[2 \[Pi] t (r + \[Delta])] +
14         2 E^(-(((c + i) \[Pi] r t)/(c i)))
15          i r Sin[2 \[Pi] r t] + (c - i) r Sin[
16         2 \[Pi] t (r + \[Delta])])^2 + (2 E^(-(((c + i) \[Pi] r
    t)/(
17          c i))) i r Cos[2 \[Pi] r t] + (c - i) r Cos[
18         2 \[Pi] t (r + \[Delta])] -
19        2 c i \[Delta] Sin[2 \[Pi] t (r + \[Delta])])^2]]
20 Manipulate[
21  Plot[{R[t, i, r, c, \[Delta]]}, {t, 0, 2.4},
22   PlotRange -> {0, 1}], {{i, 600}, 100, 1000}, {{r, 500}, 100,
23   1000}, {{c, 500}, 100, 1000},
24  {{\[Delta], 0}, -1, 1}]
25 R4 = ((c - i)^2 r^2 + 4 E^(-((2 (c + i) \[Pi] r t)/(c i))) i^2 r
    ^2 +
26    4 c^2 i^2 \[Delta]^2 -
27    4 E^(-(((c + i) \[Pi] r t)/(c i)))
28      i r (-(c - i) r Cos[2 \[Pi] t \[Delta]] +
29       2 c i \[Delta] Sin[2 \[Pi] t \[Delta]]))/((c + i)^2 r^2 +
30    4 c^2 i^2 \[Delta]^2)
```

```
31 TrueQ[Expand[R3] == Expand[R4]]
```

Listing 3: Mathematica Script for the analytical expression of the transient resonator behaviour allowing a detuned drive.

References

[1] M. H. Devoret and R. J. Schoelkopf. "Superconducting Circuits for Quantum Information: An Outlook". In: *Science* 339.6124 (2013), pp. 1169–1174.

[2] Alexandre Blais et al. "Cavity quantum electrodynamics for superconducting electrical circuits: An architecture for quantum computation". In: *Physical Review A* 69.6 (2004).

[3] C. Axline et al. "An architecture for integrating planar and 3D cQED devices". In: *Applied Physics Letters* 109.4 (2016), p. 042601.

[4] J. Majer et al. "Coupling superconducting qubits via a cavity bus". In: *Nature* 449.7161 (Sept. 2007), pp. 443–447.

[5] Chad Rigetti et al. "Superconducting qubit in a waveguide cavity with a coherence time approaching 0.1 ms". In: *Physical Review B* 86.10 (2012).

[6] R. Barends et al. "Superconducting quantum circuits at the surface code threshold for fault tolerance". In: *Nature* 508 (2014), pp. 500–503.

[7] Matthew Reagor et al. "Quantum memory with millisecond coherence in circuit QED". In: *Physical Review B* 94.1 (July 2016), p. 014506.

[8] Matthew Reagor et al. "Reaching 10 ms single photon lifetimes for superconducting aluminum cavities". In: *Applied Physics Letters* 102 (19 2013), pp. 1–5.

[9] D.M. Pozar. *Microwave Engineering, 4th Edition*. Wiley, 2011.

[10] Matthew James Reagor. "Superconducting Cavities for Circuit Qantum Electrodynamics". PhD thesis. Yale University, 2015.

[11] J. Gao. "The physics of superconducting microwave resonators PhD thesis". PhD thesis. California Institute of Technology, 2008.

[12] Jochen Braumüller. *Quantum simulation experiments with superconducting circuits*. KIT Scientific Publishing, Karlsruhe, 2018.

[13] Agustín Palacios-Laloy. "Superconducting qubit in a resonator: Test of the Leggett-Garg inequality and single-shot readout". PhD thesis. CEA Saclay, 2010.

[14] Jacob Blumoff. "Multiqubit Experiments in 3D Circuit Quantum Electrodynamics". PhD thesis. Yale University, 2017.

[15] ANSYS. *HFFS*. URL: https://www.ansys.com/products/electronics/ansys-hfss.

[16] Jonas Zmuidzinas. "Superconducting Microresonators: Physics and Applications". In: *The Annual Review of Condensed Matter Physics* 3 (2012), pp. 169–214.

[17] Kurtis Lee Geerlings. "Improving Coherence of Superconducting Qubits and Resonators". PhD thesis. Yale University, 2013.

[18] David Zöpfl. "Characterisation of stripline resonators in a waveguide". MA thesis. Universität Innsbruck, 2017.

[19] A. Bruno et al. "Reducing intrinsic loss in superconducting resonators by surface treatment and deep etching of silicon substrates". In: *Applied Physics Letters* 106.18 (May 2015).

[20] Rudolf Gross and Achim Marx. *Festkörperphysik*. Oldenbourg Verlag, 2012.

[21] O. Çakır, H. Temel, and M. Kiyak. "Chemical etching of Cu-ETP copper". In: *Journal of Materials Processing Technology* 162-163 (2005), pp. 275–279.

[22] C. Jian et al. "Effects on etching rates of copper in ferric chloride solutions". In: Organizing Committee 1998 IEMT/IMC Symposium, 1998, pp. 144–148.

[23] O. Cakir. "Copper etching with cupric chloride and regeneration of waste etchant". In: *Journal of Materials Processing Technology* 175.1-3 (2006), pp. 63–68.

[24] F.J. Humphreys and M. Hatherly. "Introduction". In: *Recrystallization and Related Annealing Phenomena (Second Edition)*. Ed. by F.J. Humphreys and M. Hatherly. Second Edition. Oxford: Elsevier, 2004, pp. 1 –10.

[25] O. Gargiulo et al. "Fast flux control of 3D transmon qubits using a magnetic hose". In: *arXiv:1811.10875 [cond-mat, physics:quant-ph]* (June 2019). arXiv: 1811.10875.

[26] Nutrien Corp. *Bright Dipping Aluminum*. 2018.

[27] Jiansong Gao et al. "Experimental evidence for a surface distribution of two-level systems in superconducting lithographed microwave resonators". In: *Applied Physics Letters* 92.15 (2008).

[28] K Saito. "Temperature Dependence of the Surface Resistance of Niobium at 1300 MHz - Comparison to BCS Theory -". In: (1999), p. 6.

[29] D. Zoepfl et al. "Characterization of low loss microstrip resonators as a building block for circuit QED in a 3D waveguide". In: *AIP Advances* 7.8 (2017), p. 085118.

[30] Knobloch J. Padamsee H. and Hays T. *RF Superconductivity for Accelerators*. Wiley series in beam physics and accelerator technology. Wiley, 1998.

[31] A. Romanenko and D. I. Schuster. "Understanding Quality Factor Degradation in Superconducting Niobium Cavities at Low Microwave Field Amplitudes". In: *Physical Review Letters* 119.26 (Dec. 2017).

[32] Burrill. "Buffer Chemical Polishing and RF Testing of the 56 MHz SRF Cavity". In: (Nov. 2019).

[33] P Kneisel. "Surface Preparation of Niobium". In: (1980), p. 14.

[34] V Palmieri, F Stivanello, and S Y Stark. "Besides the Standard Niobium Bath Chemical Polishing". In: (2001), p. 5.

[35] Yoochul Jung et al. "Analysis of BCP Characteristics for SRF Cavities". In: *Proceedings of the 5th Int. Particle Accelerator Conf.* IPAC2014 (2014).

[36] A. Romanenko et al. "Three-dimensional superconducting resonators at $T<20$ mK with the photon lifetime up to $\tau = 2$ seconds". In: *arXiv:1810.03703 [cond-mat, physics:physics, physics:quant-ph]* (Oct. 2018).

[37] David P. Pappas et al. "Two Level System Loss in Superconducting Microwave Resonators". In: *IEEE Transactions on Applied Superconductivity* 21.3 (2011), pp. 871–874.

[38] G.K White. "Thermal expansion of vanadium, niobium, and tantalum at low temperatures". In: *Cryogenics* 2.5 (1962), pp. 292–296.

[39] Gerd Schulz. *Regelungstechnik: Grundlagen, Analyse und Entwurf von Regelkreisen, rechnergestützte Methoden*. de. Springer-Lehrbuch. Berlin: Springer, 1995.

[40] Wolfram Research, Inc. *Mathematica, Version 12.0*. URL: https://www.wolfram.com/mathematica.